Asymptotic dynamic modeling and response of hysteretic nanostructured beams

Giovanni Formica [ID] · **Walter Lacarbonara** [ID]

Abstract The nonlinear dynamic response of carbon nanotube (CNT)/polymer nanocomposite beams to harmonic base excitations is investigated asymptotically via the method of multiple scales. The hysteresis associated with the CNT/polymer interfacial frictional sliding is described by a 3D mesoscopic theory reduced via a uniaxial strain assumption for a beam in pure plane bending. Such reduction leads to a Bouc–Wen-like hysteretic moment–curvature relationship. The generalized memory-dependent constitutive law is developed asymptotically and, subsequently, introduced in two archetypal cases of nonlinear beam models. A beam model is tailored for axially restrained, extensible beams (e.g., hinged–hinged beams) for which the dominant geometric nonlinearity is associated with the multiplicative effect of the tension with the bending curvature. The second model is valid for inextensible beams (e.g., cantilever beams) dominated by inertia and curvature nonlinearities. The piece-wise integration of the moment–curvature relationship yields an exponential law which is treated asymptotically to obtain the quadratic and cubic curvature contributions. The ensuing asymptotic equations of motion in the unknown deflection field are discretized according to the Galerkin method employing the eigenmode directly excited near its primary resonance to thus obtain a piece-wise reduced-order model (ROM). The method of multiple scales applied to the ROM yields the asymptotic response together with the frequency response functions for the lowest mode. A parametric study unfolds rich nonlinear dynamic responses in terms of behavior charts highlighting regions of hardening and softening behavior, regions of single-valued stable behavior and regions of multi-valued multi-stable behavior. Such richness of responses is caused by the unusual and unique combination of material and geometric nonlinearities.

1 Introduction

Nanocomposite materials are regarded as high-performance structural materials for demanding applications in dynamic environments. Lightweight nanocomposites, made of engineering (thermoplastic or thermosetting) polymers integrated with various 0D/1D/2D carbon nanofillers, are being employed to realize dynamic devices, such as microresonators, microac-

G. Formica (✉)
Dipartimento di Architettura, Roma Tre University, via Madonna dei Monti 40, Roma, Italy
e-mail: giovanni.formica@uniroma3.it

W. Lacarbonara
Department of Structural and Geotechnical Engineering, Sapienza University of Rome, via Eudossiana 18, Roma, Italy
e-mail: walter.lacarbonara@uniroma1.it

celerometers, and chemical and biosensors [1–4]. Moreover, an increasing number of works are addressing the interesting nonlinear properties of CNT-reinforced polymer materials via extensive experimental testing and analysis of 1D (i.e., ropes, beams) and 2D (i.e., plates, shells) samples [5–7] toward a wider exploitation of these new materials in aerospace, automotive, and civil engineering.

Some of the distinguished mechanical properties of CNT nanocomposite materials are the strong dependence of the storage and loss moduli on the CNT weight fraction and the nonlinear dependence of these moduli from the strain/stress levels. The dissipative capability of CNT nanocomposites is primarily attributed to a stick-slip frictional sliding motion of the long polymer molecular chains surrounding the CNTs which is triggered when the shear stresses on the CNTs outer walls overcome the interfacial shear strength. Significant interfacial shear stress jumps are caused by the severe elastic mismatch between CNTs and the hosting polymer matrix. (The Young modulus is of the order of 1000 GPa for CNTs, while it is 2–5 GPa for engineering polymers.)

The interfacial stick-slip behavior gives rise to hysteresis in the mechanical response [6–9]. This hysteretic behavior becomes increasingly more influential as more interfacial surface area becomes available for the frictional slippage. It is reported that for high-aspect-ratio, single-walled CNTs, the interfacial surface area is of the order of 500 m^2 for 1 g of CNTs. Of course, the interfacial surface area increases with the CNTs content and the CNTs aspect ratio, as previously observed in [6,7]. The hysteretic phenomenon combined with the viscosity of the polymer system typically yields a softening nonlinearity in the material dynamic response, as it happens for a variety of other strain-softening materials as well as physical/mechanical systems [10] or structures with initial curvature [11].

In a preliminary work [12], the nonlinear dynamic response of nanocomposite cantilevers (made of thermoplastic polybutylene terephthalate polymer and single-walled CNTs) was experimentally investigated and compared with the response of a neat polymer beam subject to a primary resonance base excitation. A key result was the switch from softening- to hardening-type nonlinearity. This was attributed to the competing softening effects induced by the nanostructural stick-slip with the hardening effects due to the nonlinear curvature. An initial mechanical model for nanocom-

posite beams was proposed considering the nonlinear Euler–Bernoulli beam theory projected onto the excited mode according to the Galerkin method. The obtained reduced-order equation of motion was thus modified to account for a generalized hysteretic force regulated by a modified Bouc–Wen model of hysteresis. The qualitative features of the experimental frequency response curves were thus reproduced as documented in [12].

In the present work, we derive consistent models of nanocomposite beams via a suitable reduction of the 3D nanocomposite mesoscale constitutive model [13,14] facilitated by the uniaxial strain state ansatz for the assumed plane bending case treated to obtain the moment–curvature relationship. A phenomenological 1D model obtained as a by-product of the full 3D model was also shown to provide results in agreement with experiments [15].

Here we discuss two nanocomposite beam models valid for (1) axially restrained, unshearable/extensible beams and (2) for unshearable/inextensible beams. Subsequently, an unusual mix of the Galerkin discretization approach with a suitable asymptotic treatment leads to a reduced-order model in which the restoring force has a piece-wise representation in each of the four branches of the hysteresis loops. The obtained piece-wise ODE is further attacked by the method of multiple scales to obtain the asymptotic periodic solutions and the associated frequency response functions for the primary resonance of the lowest mode. A predecessor of this work about the effects of material nonlinearities is [16] where a nonlinearly viscoelastic moment–curvature relationship was defined to study the influence of polynomial-type material nonlinearities on flexural vibrations of circular rings.

The method of multiple scales [17] is widely employed to study the frequency response and bifurcations of a variety of nonlinear systems for increasing levels of approximation. In [16,18,19], the nonlinear dynamic behavior of distributed parameter systems with quadratic and cubic nonlinearities, including cables/beams/rings, was investigated. A similar asymptotic approach was employed in [20,21] to study the dynamic response of a nonlinear hysteretic vibration absorber (with and without pinching) alone and together with a primary system, its stability and sensitivity with respect to the constitutive parameters. In the present work, the wide tunability of the nonlinear dynamic response of nanocomposite beams which combine material and geometric nonlinearities is stud-

ied thanks to the computational versatility afforded by the asymptotic solutions. The present study into the dynamic response of infinite-dimensional systems is framed within the stream of works dealing with one- or two-degree-of-freedom systems exhibiting bilinear hysteresis [22], yielding structures [23], degrading systems [24] and other hysteretic systems [25–37] improved to better capture the complexities of different nonlinearities including shape memory phase transitions coupled with thermomechanical features [38,39].

The paper is organized as follows. Section 2 discusses the nonlinear nanocomposite beam models whose discretization and asymptotic treatment are detailed in Sect. 3. The asymptotic treatment and the main results are illustrated in Sects. 4 and 5, respectively.

2 Nonlinear nanocomposite beam models

A geometrically exact (Euler–Bernoulli) model of nanocomposite beams in plane bending is chosen as the baseline beam model together with an *ad hoc* nonlinear constitutive formulation whose tailoring and computational implementation represent the main modeling challenge. In the linear material range, equivalent stress–strain relationships relating, in a Mori-Tanaka sense, average stresses with average strains are already available [5]. On the other hand, the relative CNT/polymer frictional sliding occurring when the localized interfacial shear stresses overcome the shear strength introduces a strong nonlinearity in the stress–strain relationships. Such a "stick-slip" behavior between the two phases was described by a mescoscale nonlinear constitutive model [13,14] valid for uniformly aligned CNTs. A phenomenological derivation of the 3D model was experimentally validated in [15]. The same 3D nanocomposite model was employed for optimization studies seeking to maximize at the same time damping and stiffness of multilayer nanocomposite plates in [40,41]. A generalization for randomly oriented CNTs and accounting for nonuniform CNT aspect ratios was proposed and experimentally validated in [42].

The 3D mesoscale model suitably reduced to account for a plane bending problem (a linear counterpart was proposed in [2]) together with the Saint-Venant ansatz is employed to obtain a generalized constitutive law

which regulates the bending moment variation with the beam bending curvature.

Nonlinear constitutive model for CNT/polymer nanocomposites. The considered nanocomposites are made of two material phases, the hosting polymer matrix (here and henceforth denoted by subscript "m") and the CNTs (denoted by subscript "c") modeled as cylindrical inclusions [13]. According to the Mori–Tanaka approach, the nanocomposite stresses and strains are assumed as averaged continuum tensors of the two phases (i.e., the so-called *rule of mixture*) treated separately as two continuum media, $\dot{T} = \phi_m \dot{T}_m + \phi_c \dot{T}_c$ and $\dot{E} = \phi_m \dot{E}_m + \phi_c \dot{E}_c$ where the scalar ϕ_c is the CNT volume fraction and $\phi_m := 1 - \phi_c$ is that of the hosting matrix.

Here we adopt Gibbs notation for vector and tensor fields. In particular, the dot and cross products of vectors u and v are denoted by $u \cdot v$ and $u \times v$, respectively. The image T of second-order tensor E under the application of fourth-order tensor $\mathbf{L}$ is expressed as $T = \mathbf{L} : E$, i.e., $T_{ij} = L_{ijhk} E_{hk}$. The same notation is employed to indicate the inner tensor product between both second- and fourth-order tensors, namely $T : E$ and $\mathbf{A} : \mathbf{B}$, respectively; these inner products are expressed as $T : E = T_{ij} E_{ij}$ and $\mathbf{A} : \mathbf{B} = A_{ijhk} B_{hklm}$. The tensor product between second-order tensors reads finally as $T \otimes E = T_{ij} E_{hk}$.

According to Hill's approach [43], phase-strain tensors can be mapped into equivalent strains as

$$\dot{E}_m = \mathbf{A}_m : \dot{E}, \quad \dot{E}_c = \mathbf{A}_c : \dot{E}, \tag{1}$$

where the fourth-order tensors $\mathbf{A}_m$ and $\mathbf{A}_c$ (called the dilute mechanical strain concentration tensors such that $\phi_m \mathbf{A}_m + \phi_c \mathbf{A}_c = \mathbf{I}$) account for Eshelby's theory of equivalent inclusion, together with the stress interface conditions; they thus depend on both the equivalent stress and strain for a given nonlinear constitutive law.

Both the hosting matrix and the CNTs are treated as linearly elastic, isotropic continuum media, while the constitutive nonlinearity is introduced at the interface level; that is,

$$\dot{T}_m = \mathbf{L}_m : \dot{E}_m, \quad \dot{T}_c = \mathbf{L}_c : \dot{E}_c \tag{2}$$

where $\mathbf{L}_m$ and $\mathbf{L}_c$ are the fourth-order tensors of elastic coefficients of the two isotropic phases which depend

on Young's moduli (E_m, E_c) and Poisson's ratios (ν_m, ν_c), respectively.

The equivalent constitutive law is then obtained by combining the rule of mixture with (2), together with the equilibrium at the interface and the Eshelby inclusion governed by Eshelby's tensor **S** incorporating the shape, geometry, and variability of the CNTs length within the nanocomposite [13,42]. The nanocomposite equivalent stress–strain relationships are thus given by $\dot{T} = \mathbf{L} : \dot{E}$ in which the equivalent elastic tensor is defined as

$$\mathbf{L} = \mathbf{L}_m + \phi_c \langle (\mathbf{L}_c - \mathbf{L}_m) : \mathbf{A}_c \rangle (\phi_m \mathbf{I} + \phi_c \langle \mathbf{A}_c \rangle)^{-1} \quad (3)$$

where **I** is the identity tensor while the dilute mechanical strain concentration tensor $\mathbf{A}_c$ is given by

$$\mathbf{A}_c = \left[\mathbf{I} + \mathbf{S} : (\mathbf{L}_m)^{-1} : (\mathbf{L}_c - \mathbf{L}_m) \right]^{-1}. \quad (4)$$

Here **S** is specialized to account for the assumed cylindrical geometry of the CNTs. To introduce the CNT orientation, which may be aligned with a preferential direction or be random throughout the medium, the terms enclosed by angle brackets indicate the tensor transformation from the local CNT-fixed frame to the global frame ($\langle \mathbf{A}_c \rangle = \mathbf{R}^\top : \mathbf{A}_c : \mathbf{R}$ accounting for the relative rotation about a prescribed coordinate axis in case of CNTs collinear with a given direction) as well as the additional averaging operation over all orientations in the case of random CNTs. Tensor **R** represents the rotation parametrized, for example, by Euler's angles.

For perfectly aligned CNTs depicted in Fig. 1, the equivalent constitutive law is simplified into

$$\dot{T} = \left[\phi_m \, \mathbf{L}_m : \mathbf{A}_m + \phi_c \, \mathbf{L}_c : \mathbf{A}_c \right] : \dot{E}$$
$$= \mathbf{L}_m : \dot{E} + \phi_c \left[\mathbf{L}_c - \mathbf{L}_m \right] : \mathbf{A}_c : \dot{E} \quad (5)$$

As proposed in [13,14], the hysteretic stick-slip behavior is framed within the same context of the above described Eshelby–Mori–Tanaka approach developed in linear elasticity. The constitutive law is obtained introducing a smooth transition from the stick to the slip condition according to a Bouc–Wen-like law:

$$\dot{T}_c = \widehat{\mathbf{L}}_c(T_c) : \dot{E}_c = \mathbf{L}_c : \dot{E}_c$$
$$- 3\mu_c \, \widehat{s}(T_c : \dot{T}_c) \left(\frac{\Phi(T_c)}{S_o} \right)^{n-2} \left[\frac{T_c^{\mathrm{dev}}}{S_o} \otimes \frac{T_c^{\mathrm{dev}}}{S_o} \right] : \dot{E}_c \quad (6)$$

where $\Phi(T_c)$ is the von Mises function of the CNT-phase stress which the interfacial stress discontinuity depends on [14]:

$$\Phi(T_c) := \sqrt{\frac{3}{2} \, T_c^{\mathrm{dev}} : T_c^{\mathrm{dev}}}, \quad \widehat{s}(T_c : \dot{T}_c)$$
$$:= \beta + \gamma \, \mathrm{sign}(T_c : \dot{T}_c). \quad (7)$$

with n, β, and γ denoting the classical Bouc–Wen parameters and T_c^{dev} the deviatoric part of the stress tensor jump at the interface.

Due to the highly nonlinear nature of the 3D constitutive law, a rigorous 1D reduction is a complex task. However, a simplified 1D model mimicking the 3D constitutive law was proven to yield results
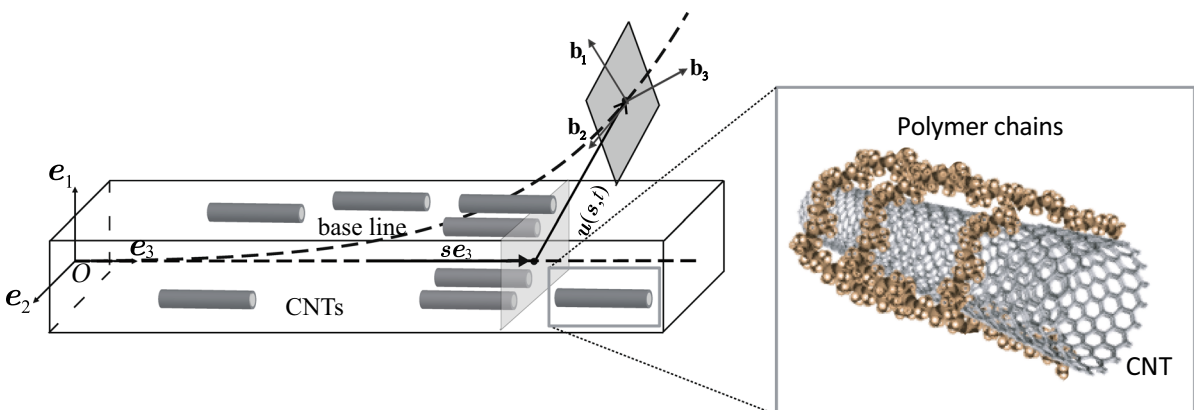

Fig. 1 Carbon nanotube nanocomposite beam model. The arclength along the base line is denoted by s while the displacement vector $\mathbf{u}(s, t)$ describes the current position of the base point of the cross sections

in qualitative agreement with the experimental data [15].

Consider the limit condition in which the von Mises function reaches asymptotically the interfacial shear strength S_o read in the CNT phase (i.e., onset of slip), namely $\Phi(\boldsymbol{T}_c) \to S_o$. This condition occurs when $\dot{\Phi}(\boldsymbol{T}_c) \to 0$. This implies necessarily $\boldsymbol{T}_c^{\mathrm{dev}} : \dot{\boldsymbol{T}}_c^{\mathrm{dev}} \to 0$, hence, $\boldsymbol{T}_c^{\mathrm{dev}} \to c\,\mathbf{I}$ with $c = S_o \sqrt{2}/3$. At the onset of the slip phase, the constitutive law (6) thus becomes

$$\dot{\boldsymbol{T}}_c \to \mathbf{L}_c : \dot{\boldsymbol{E}}_c - \frac{2}{3}\mu_c\,[\mathbf{I} \otimes \mathbf{I}] : \dot{\boldsymbol{E}}_c$$
$$\equiv \bar{\lambda}_c\,\mathrm{tr}(\dot{\boldsymbol{E}}_c)\,\mathbf{I} + 2\,\mu_c\,\dot{\boldsymbol{E}}_c \qquad (8)$$

where $\bar{\lambda}_c := (\lambda_c - \frac{2}{3}\mu_c)$ is the reduced Lamé constant of the CNT phase. On the other hand, the linearized law about the origin (i.e., linearly elastic law) is given by $\dot{\boldsymbol{T}}_c = \lambda_c\,\mathrm{tr}(\dot{\boldsymbol{E}}_c)\,\mathbf{I} + 2\,\mu_c\,\dot{\boldsymbol{E}}_c$. Thus, we can rewrite the linearized constitutive equations, valid at the origin and in the post-slip condition, as $\dot{\boldsymbol{T}}_c = \lambda_c^{(i)}\,\mathrm{tr}(\dot{\boldsymbol{E}}_c)\,\mathbf{I} + 2\,\mu_c\,\dot{\boldsymbol{E}}_c$ where $\lambda_c^{(1)} = \lambda_c$ for the elastic tangent case and $\lambda_c^{(2)} = \bar{\lambda}_c$ for the post-slip case.

1D reduction process of the full constitutive law. For the plane-bending problem here considered, we assume the elongation E_{33} in the $\mathbf{e}_3$ direction as the only nontrivial strain component, that is, $E_{ij} = 0$ for any $i \neq 3, j \neq 3$ and $E_{33} \neq 0$ (see Fig. 1). According to Voigt's notation, the strain tensor components can be collected in the strain vector $\boldsymbol{\epsilon} = (0, 0, E_{33}, 0, 0, 0)$ and the stresses in the stress vector $\boldsymbol{\sigma} = (T_{11}, T_{22}, T_{33}, T_{13}, T_{23}, T_{12})$. The constitutive equation $(2)_2$ of the CNT phase can be rewritten using Eq. $(1)_2$; the obtained expressions keep the same format in both tangent and limit conditions, $\dot{\boldsymbol{T}}_c = \mathbf{L}_c : \mathbf{A}_c : \dot{\boldsymbol{E}}$. The stress vector $\boldsymbol{\sigma}_c$ can be simplified into

$$\dot{\boldsymbol{\sigma}}_c = \frac{1}{\lambda_c^{(i)} + \mu^+} \begin{bmatrix} \lambda_m \mu_c + \lambda_c^{(i)}(\lambda_m + \mu_m) \\ \lambda_m \mu_c + \lambda_c^{(i)}(\lambda_m + \mu_m) \\ 2\mu_c \mu^+ + \lambda_c^{(i)}(\lambda_m + \mu_m + 3\mu_c) \\ 0 \\ 0 \\ 0 \end{bmatrix} \dot{E}_{33} \qquad (9)$$

where $\mu^+ := \mu_c + \mu_m$. In the same way, the equivalent constitutive law can be expressed as

$$\dot{\boldsymbol{\sigma}} = \begin{bmatrix} \lambda_m \\ \lambda_m \\ \lambda_m + 2\mu_m \\ 0 \\ 0 \\ 0 \end{bmatrix} \dot{E}_{33}$$
$$+ \frac{1}{\lambda_c^{(i)} + \mu^+} \begin{bmatrix} \lambda_m \mu_c + \lambda_c^{(i)}(\lambda_m + \mu_m) \\ \lambda_m \mu_c + \lambda_c^{(i)}(\lambda_m + \mu_m) \\ \Delta \\ 0 \\ 0 \\ 0 \end{bmatrix} \dot{E}_{33} \qquad (10)$$

where $\Delta := \lambda_c^{(i)}(\lambda_m + \mu^- + 2\mu_c) + 2\mu^+ \mu^- - \lambda_m(\lambda_m - \mu^+)$ and $\mu^- := \mu_c - \mu_m$.

Moment–curvature relationship. First, to move toward the constitutive relationship between the generalized stress resultants and the generalized strains, we express the elongation E_{33} of a fiber at distance x_1 from axis $\boldsymbol{b}_2$ in a state of uniform extension and plane bending as $E_{33} = \epsilon - \kappa x_1$ where ϵ is the elongation of the base line and κ is the bending curvature [11]. The base line is taken to coincide with the centerline and the unit vectors $(\boldsymbol{b}_1, \boldsymbol{b}_2)$ are taken collinear with the principal axes of inertia of the cross sections (see Fig. 3). On the other hand, the stress–strain relationship of interest is obtained from (10) as $\dot{T}_{33} = E^{(i)}\dot{E}_{33}$ where the effective tangent modulus is given by

$$E^{(i)} = \lambda_c^{(i)}[\lambda_m(1 + \phi_c) + 2(\mu_c\phi_c + \mu_m) + \mu^-\phi_c]$$
$$- [\lambda_m^2\phi_c - \mu^+(\lambda_m\phi_m + 2\bar{\mu})]/\lambda_c^{(i)} + \mu^+ \qquad (11)$$

with $\bar{\mu} := (\mu_m\phi_m + \mu_c\phi_c)$. It turns out that the effective modulus $E^{(2)}$ in the post-slip condition suffers a drop with respect to the initial (elastic) modulus $E^{(1)}$ proportional to the CNT volume fraction and given by

$$[E^{(1)} - E^{(2)}] = \frac{2\mu_c(\lambda_m + \mu^+)^2}{(\lambda_c + \mu^+)(3\lambda_c + \mu_c + 3\mu_m)}\phi_c.$$

The linearized time rate of change of tension and bending moment at the origin and in the post-slip condition can be computed, respectively, as

$$\dot{N} = \int_S \dot{T}_{33}\,\mathrm{d}A = E^{(i)}A\,\dot{\epsilon},$$
$$\dot{M} = -\int_S x_1\,\dot{T}_{33}\,\mathrm{d}A = E^{(i)}J\,\dot{\kappa} \qquad (12)$$

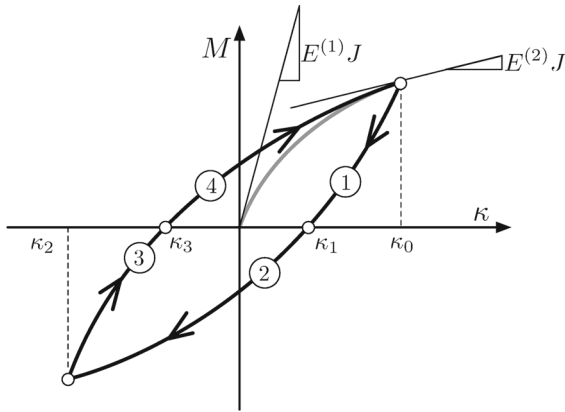where S indicates the beam cross-sectional domain.

Fig. 2 Typical bending moment–curvature hysteretic curve. For symmetric material responses, $\kappa_2 = -\kappa_0$ and $\kappa_3 = -\kappa_1$

In the plane beam models that we present in the next sections, bending is the directly induced driving strain state while stretching of the base plane is indirectly induced as a second-order strain effect, and hence it is considered to be small. Therefore, here we focus on the overall hysteretic bending–curvature constitutive law of which we computed the linearized versions given by Eq. (12) (see the tangents in Fig. 2). The constitutive law describing the bending moment in the whole range of curvatures can be expressed by mimicking the 3D law proposed in [14] and framed in the Saint-Venant theory for beams in bending [12]; that is,

$$\dot{M} = E^{(1)}J \left\{ 1 - \left(1 - \frac{E^{(2)}J}{E^{(1)}J} \right) \right.$$
$$\left. \times \left[\beta + \gamma \, \text{sign}((M - E^{(2)}J\kappa)\dot{\kappa}) \right] \left| \frac{M - E^{(2)}J\kappa}{M_o} \right|^n \right\} \dot{\kappa}$$
(13)

where M_o is the threshold bending moment at which the transition between the stick (elastic) phase and the slip (post-elastic) phase occurs in the limit $n \rightarrow \infty$. The limit moment M_o depend on the limit stress S_o.

Letting $M_z^* := (M - E^{(2)}J\kappa)/M_o$ and $\kappa^* := \kappa/\kappa_y$ with $\kappa_y := M_o/\Delta B$ and $\Delta B := (E^{(1)}J - E^{(2)}J)$, Eq. (13) becomes

$$\dot{M}/M_o = E^{(1)}J/\Delta B \dot{\kappa}^* - \left(\beta + \gamma \, \text{sign}(M_z^* \dot{\kappa}) \right) |M_z^*|^n \dot{\kappa}^*,$$
(14)

which, substituted into the rate of M_z^*, delivers

$$\dot{M}_z^* = \dot{M}/M_o - E^{(2)}J/\Delta B \dot{\kappa}^*$$
$$= \left[1 - \left(\beta + \gamma \, \text{sign}(M_z^* \dot{\kappa}^*) \right) |M_z^*|^n \right] \dot{\kappa}^*.$$
(15)

Thus the moment–curvature relationship given by Eq. (13) upon partial integration can be expressed as the classical form of the Bouc–Wen model

$$M = E^{(1)}J[\delta\kappa + (1 - \delta)\chi]$$
(16)

where $\delta := E^{(2)}J/E^{(1)}J$ is the ratio between the post-slip bending stiffness and the elastic bending stiffness and $\chi := \kappa_y M_z^*$ is the hysteretic contribution to the bending curvature given by

$$\dot{\chi} = \left[1 - \left(\bar{\beta} + \bar{\gamma} \, \text{sign}(\chi\dot{\kappa}) \right) |\chi|^n \right] \dot{\kappa}$$
(17)

with $(\bar{\beta}, \bar{\gamma}) = (\beta, \gamma)/\kappa_y^n$ where κ_y is rewritten as $\kappa_y = M^{(o)}/[(1 - \delta)E^{(1)}J]$.

Note that the nonlinear effects of the hysteresis described by Eqs. (16) and (17) can be predicted both qualitatively and quantitatively by considering variations of the average nondimensional bending stiffness with the curvature. Here the average of the bending stiffness divided by the initial tangent stiffness $E^{(1)}J$ is defined as

$$\overline{EJ} = \left[1 - (1 - \delta) \frac{\int_C \left\{ \left(\bar{\beta} + \bar{\gamma} \, \text{sign}(\chi\dot{\kappa}) \right) |\chi|^n \right\} d\kappa}{\int_C d\kappa} \right]$$

where C indicates the closed hysteresis cycles with the loading and unloading branches. Indeed, increasing or decreasing variations of $\overline{EJ}$ with the cyclic amplitude entail a hardening (softening) behavior. In the literature, it is said that the hysteresis given by Eqs. (16) and (17) is softening if $(\bar{\beta} + \bar{\gamma}) > 0$ (i.e., the stiffness degrades along the virgin loading branch), quasi-linear if $(\bar{\beta} + \bar{\gamma}) = 0$ (i.e., the stiffness does not change), and hardening if $(\bar{\beta} + \bar{\gamma}) < 0$ (i.e., the stiffness increases along the virgin loading branch).

Equations of motion for nanocomposite beams. Consider the fixed frame $(O, \mathbf{e}_1, \mathbf{e}_2, \mathbf{e}_3)$ in Fig. 3 and the restricted plane of motion described by $(O, \mathbf{e}_3, \mathbf{e}_1)$. Let s denote the material coordinate that spans the beam centerline in the reference configuration. The beam is subject to a base motion in the vertical direction (i.e, $\mathbf{e}_1$−direction). The current position of the center of the cross section is described by $\mathbf{r}(s, t) = s\mathbf{e}_3 + y(t)\mathbf{e}_1 + \mathbf{u}(s, t)$ where $y(t)\mathbf{e}_1$ is the prescribed base motion while the displacement vector relative to the moving frame is

Fig. 3 The nanocomposite beam models in plane bending: (left) hinged–hinged beam and (right) cantilever beam
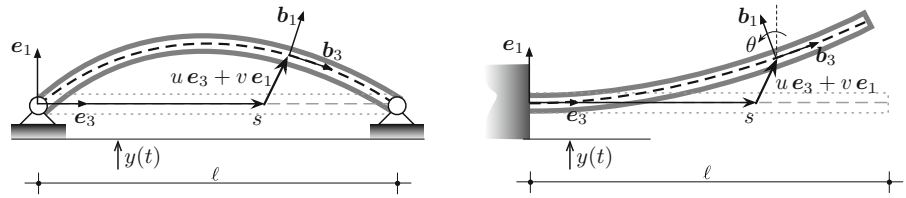
$\mathbf{u}(s, t) = u(s, t) \mathbf{e}_3 + v(s, t) \mathbf{e}_1$. Moreover, θ denotes the counterclockwise angle by which the cross section at s is flexurally rotated about $\mathbf{e}_2$.

The full derivation of the equations of motion is provided in "Appendix" for the two cases of interest, namely hinged–hinged and cantilever beams. The case of hinged–hinged beams belongs to the class of axially restrained beams, while the cantilevers are treated in line with the literature as unshearable–inextensible beams.

Extensible beams. Axially restrained beams are subject to stretching induced by the transverse motion. An approximate theory for axially restrained beams is due to Mettler and its proposed specialization to account for the hysteretic nonlinearities in the constitutive law is fully described in "Appendix". The approximate equation of motion is given by

$$\rho A \partial_{tt} v + \partial_{ss} M$$
$$- \frac{E^{(1)} A}{2\ell} \partial_{ss} v \int_0^\ell (\partial_s v)^2 \mathrm{d}s = -\rho A \partial_{tt} y + f \quad (18)$$

$$M = E^{(1)} J [\delta \kappa + (1 - \delta) \chi], \quad (19)$$

$$\partial_t \chi = \left[1 - \left(\bar{\beta} + \bar{\gamma} \, \mathrm{sign}(\chi \, \partial_t \kappa) \right) |\chi|^n \right] \partial_t \kappa \quad (20)$$

where the curvature is given by $\kappa \cong \partial_{ss} v + \frac{1}{2} (\partial_s v)^2 \partial_{ss} v$. In particular, for hinged–hinged beams, the boundary conditions are

$$v(0, t) = 0 = v(\ell, t), \ \ \partial_{ss} v(0, t) = 0 = \partial_{ss} v(\ell, t).$$

The mechanical boundary conditions are $M(0, t) = 0 = M(\ell, t)$. The boundary conditions $\partial_{ss} v = 0$ ensue from letting the third-order expansion of the curvature vanish at the beam ends.

Inextensible beams. The beam equations specialized for the shear undeformability and longitudinal inextensibility constraints (see "Appendix") are cast in the form

$$\rho A \partial_{tt} v \left[1 - \tfrac{1}{2} (\partial_s v)^2 \right]$$
$$+ \rho A \partial_s v \int_0^s \left[\partial_\xi v \partial_{\xi tt} v + (\partial_{\xi t} v)^2 \right] \mathrm{d}\xi$$
$$- \partial_{ss} v \int_s^\ell \left[\rho A \int_0^s \left[\partial_\xi v \partial_{\xi tt} v + (\partial_{\xi t} v)^2 \right] \mathrm{d}\xi \right] \mathrm{d}s$$

$$+ \partial_{ss} v \int_s^\ell \left[\rho A \partial_{tt} v \partial_\xi v \right] \mathrm{d}\xi$$
$$+ c \, \partial_t v - \partial_{ss} v \int_s^\ell \partial_{ss} v \partial_s M \mathrm{d}\xi + \partial_{ss} M = f - \rho A \, \partial_{tt} y. \quad (21)$$

The moment–curvature relationship for M is given again by Eqs. (19) and (20) and the boundary conditions are

$$v(0, t) = 0 = \partial_s v(0, t), \ \ \partial_{ss} v(\ell, t) = 0 = \partial_{sss} v(\ell, t).$$

For the cantilever beam, the mechanical boundary conditions at the beam tip require the bending moment and the shear force to vanish.

3 Discretization and asymptotic treatment

We will treat in detail the case of axially restrained beams with hinged–hinged boundary conditions, while we will present briefly the unshearable–inextensible cantilevers. We first nondimensionalize the equation of motion rescaling space and time as $s^\star = s/\ell$, $t^\star = \omega_c t$ in which the characteristic circular frequency is set as $\omega_c = \sqrt{\bar{k} \ell / (\rho A \, \ell^4)}$ where $\bar{k}$ will be determined at a later stage to simplify the asymptotic analysis. The deflection is also rescaled as $v^* := v/\ell$, and for conciseness, the notation $\partial_s g = 1/\ell \, g'$ and $\partial_t g = \omega_c \dot{g}$ is introduced for any function g, thus letting the prime and the overdot indicate differentiation with respect to $s^\star$ and $t^\star$, respectively.

The nondimensional equation of motion (18) thus becomes

$$\ddot{v}^* + 2 \zeta \, \dot{v}^* - \frac{E^{(1)} A \, \ell}{2\bar{k}} \, v^{*\prime\prime} \int_0^1 (v^{*\prime})^2 \mathrm{d}s^\star + \frac{1}{\bar{k}} M'' = -\ddot{y}. \quad (22)$$

It can also be recast according to the classical D'Alembert principle as a balance between inertia (f_i), damp-

ing (f_d), restoring (f_r) forces and the excitation p in the form $f_i + f_d + f_r - p = 0$ with

$$f_i = \ddot{v}^*, \quad f_d = 2\zeta\, \dot{v}^*, \quad f_r = f_m + f_g,$$
$$f_m = \frac{1}{\bar{k}} M'', \quad f_g = -\frac{E^{(1)} A\,\ell}{2\bar{k}} v^{*\prime\prime} \int_0^1 (v^{*\prime})^2 ds^\star,$$
$$p = -\ddot{y} \tag{23}$$

where f_m stands for the nonlinear hysteretic force and f_g indicates the geometrically nonlinear restoring force.

We subsequently apply the Galerkin discretization method retaining one mode only in the approximate expression for the deflection. Such simplifying assumption is plausible because the resulting generalized (hysteretic) restoring force–displacement relationship is symmetric with respect to the origin and thus the fundamental periodic oscillations of the harmonically excited beams are expected to be symmetric (i.e., without drift) about the rest (straight) equilibrium. As known in the literature, spatially continuous, symmetric systems (i.e., endowed with a symmetric potential energy function) can be well approximated by the directly excited mode via a primary resonance excitation [44].

The one-mode approximation reads $v^*(s^\star, t^\star) = q_j(t^\star)\,\phi_j(s^\star)$ where the normalized jth mode shape of the hinged–hinged beam is

$$\phi_j(s^\star) = \sqrt{2}\,\sin(j\pi s^\star), \quad j \in \mathbb{N} \tag{24}$$

such that $\int_0^1 \phi_j\,\phi_j\;ds^\star = 1$. The nondimensional jth frequency is given by

$$\omega_j^2 = (j\pi)^4 \frac{E^{(1)} J}{\bar{k}\ell}.$$

We make the additional assumption that the frequency of the first mode becomes unitary (i.e., $\omega_1 = 1$) so that

$$\bar{k} := \pi^4 \frac{E^{(1)} J}{\ell}. \tag{25}$$

The reduced-order model is obtained projecting each term of the equation of motion, say f_h, onto the mode shape ϕ_j according to

$$\int_0^1 f_h \phi_j\,ds^* =: \mathcal{D}_j[f_h]$$

where, for ease of notation, $\mathcal{D}_j[\cdot]$ was introduced to indicate the projection operator onto the jth mode.

Asymptotic expressions of the discretized restoring force. The restoring force associated with the material nonlinearity in both beam models involves differentiation of the bending moment with respect to the arclength s^*. Note that the hysteretic part of the curvature can be obtained in closed form integrating Eq. (20) with $n = 1$, and accounting for $\mathrm{sign}(\chi\,\partial_t\kappa) = \pm 1$ and $|\chi| = \pm 1$ on each of the four branches of the hysteresis loops (see Fig. 2). Four expressions of the hysteretic curvature can thus be obtained on each of the corresponding branches. To this end, Eq. (20) can be first recast as

$$\frac{\partial \chi_l}{\partial \kappa} = (1 + s_l\,\chi_l), \quad l = 1, \ldots, 4$$

where s_l denotes the lth component of $\mathbf{s} = (\bar{\gamma} - \bar{\beta},\ \bar{\gamma} + \bar{\beta},\ -\bar{\gamma} + \bar{\beta},\ -\bar{\gamma} - \bar{\beta})$ (i.e., the set of constitutive parameters combinations defined on each branch) and χ_l is the hysteretic curvature defined on the lth branch. The above equation can thus be solved analytically to yield

$$\chi_l = -\frac{1}{s_l} + c_l \exp(s_l\,\kappa). \tag{26}$$

By letting κ_0 and κ_2 be the values of the curvatures at which χ reaches the upper and lowers bounds, respectively, and κ_1 and κ_3 be the values of the curvatures at which χ vanishes, that is, crosses the positive and negative κ−semi-axes, respectively, the rescaled hysteretic moment–curvature cycle $(\chi,\ \kappa)$ is made of four branches, each bounded by two points:

$$\big(\kappa_{l-1},\, \chi_l(\kappa_{l-1})\big),\ \ \big(\kappa_l,\, \chi_l(\kappa_l)\big),$$
for any branch $l = 1,\ 2,\ 3,\ 4.$

The characteristic curvatures $(\kappa_0, \kappa_1, \kappa_2, \kappa_3)$ are not independent in force of the symmetry of the cycle which requires $\kappa_2 = -\kappa_0$ and $\kappa_3 = -\kappa_1$: the independent curvatures are then κ_0 and $\kappa_1 =: \kappa_\mathrm{C}$. The four coefficients c_l in Eq. (26) are determined as function of κ_C by imposing the following four conditions:

$$\chi_1(\kappa_\mathrm{C}) = 0 = \chi_2(\kappa_\mathrm{C}), \quad \chi_3(-\kappa_\mathrm{C}) = 0 = \chi_4(-\kappa_\mathrm{C}),$$

together with the branch-to-branch continuity conditions:

$$\chi_1(\kappa_0) - \chi_4(\kappa_0) = 0, \quad \chi_2(-\kappa_0) - \chi_3(-\kappa_0) = 0.$$

We next expand in series of ϵ (i.e., a formal bookkeeping parameter) the curvature as $\kappa = \epsilon\kappa_1 + \epsilon^2\kappa_2 + \epsilon^3\kappa_3$ together with the characteristic curvatures κ_C and κ_0 as

$\kappa_C = \epsilon \kappa_{C1} + \epsilon^2 \kappa_{C2} + \epsilon^3 \kappa_{C3}$ and $\kappa_0 = \epsilon \kappa_{01} + \epsilon^2 \kappa_{02} + \epsilon^3 \kappa_{03}$. We then substitute these expansions in the above two inter-branch continuity equations which, in turn, can be solved to yield κ_{Ci} in terms of κ_{0i}. In this way, the piece-wise description of the hysteretic cycle is given at each order in terms of κ_{0i} and κ_i.

We thus express the bending moment for each branch as

$$M_l = E^{(1)} J \left[\delta \kappa + (1 - \delta) \chi_l \right]$$
$$= E^{(1)} J \left[\kappa + (1 - \delta) \chi_l^{\mathrm{nl}} \right] \tag{27}$$

where $\chi_l^{\mathrm{nl}} := \chi_l - \kappa$ is the purely nonlinear part of the hysteretic curvature. Subsequently, the obtained piece-wise nonlinear part of the hysteretic curvature upon expansion in Taylor series of ϵ reads

$$\chi_l^{\mathrm{nl}} = \epsilon^2 \chi_{2l}^{\mathrm{nl}} + \epsilon^3 \chi_{3l}^{\mathrm{nl}}$$

where

$$\chi_{2l}^{\mathrm{nl}} = c_{1l} \kappa_{01}^2 + c_{2l} \kappa_1^2, \quad \chi_{3l}^{\mathrm{nl}} = d_{1l} \kappa_{01} \kappa_{02} + d_{2l} \kappa_1 \kappa_2$$
$$+ d_{3l} \kappa_{01}^3 + d_{4l} \kappa_{01}^2 \kappa_1 + d_{5l} \kappa_1^3.$$

The coefficients (c_{jl}, d_{jl}) are listed in Table 1.

The bending curvature κ is expressed in terms of the deflection v as

$$\kappa \cong \partial_{ss} v + \tfrac{1}{2} (\partial_s v)^2 \partial_{ss} v = \left[v^{*''} + \tfrac{1}{2} (v^{*'})^2 v^{*''} \right] / \ell.$$

Moreover, the expression of the deflection based on the one-mode approximation, $v^*(s^\star, t^\star) = q_j(t^\star) \phi_j(s)$, is expanded in Taylor series of ϵ. To this end, here and henceforth, we will drop the subscript j in ϕ_j and q_j, as well as in $\mathcal{D}_j$, while the newly introduced subscript i in q_i will indicate the ith order of the asymptotic expansion. Therefore, substituting

$$q = \epsilon q_1 + \epsilon^2 q_2 + \epsilon^3 q_3 \tag{28}$$

into the discretized deflection and the bending curvature κ yields the expansion of the hysteretic restoring force $f_{m,l} := M''/(\ell \bar{k}) = E^{(1)} J/(\ell \bar{k})[\kappa'' + (1 - \delta)(\chi_l^{\mathrm{nl}})'']$ in the following piece-wise form:

$$f_{m,l} \approx \frac{E^{(1)} J}{\ell \bar{k}} \left\{ \left(\epsilon q_1 + \epsilon^2 q_2 + \epsilon^3 q_3 \right) \phi'''' \right.$$
$$+ \epsilon^3 q_1^3 \left[(\phi'')^3 + \tfrac{1}{2} (\phi')^2 \phi'''' + 3 \phi' \phi'' \phi''' \right]$$
$$+ \epsilon^2 (1 - \delta) 2 \left((\phi''')^2 + \phi'' \phi'''' \right)$$
$$\left(\frac{c_{1l}}{\ell} q_{01}^2 + \frac{c_{2l}}{\ell} q_1^2 \right)$$
$$+ \epsilon^3 (1 - \delta) \left[2 \left((\phi''')^2 + \phi'' \phi'''' \right) \right.$$
$$\left(\frac{d_{1l}}{\ell} q_{01} q_{02} + \frac{d_{2l}}{\ell} q_1 q_2 \right)$$
$$+ 3 \phi'' \left(2(\phi''')^2 + \phi'' \phi'''' \right)$$
$$\left. \left. \left(\frac{d_{3l}}{\ell^2} q_{01}^3 + \frac{d_{4l}}{\ell^2} q_{01}^2 q_1 + \frac{d_{5l}}{\ell^2} q_1^3 \right) \right] \right\}.$$

The obtained restoring force per unit reference beam length associated with the shear/bending load-carrying mechanism is present in both extensible and inextensible beams. However, the actual computation of the total restoring forces which include the material and geometric/inertia nonlinearities differs depending on whether the beam is extensible or inextensible. We provide next the results for hinged–hinged beams.

Hinged–hinged beams. The discrete form of the restoring force, including the material and geometric nonlinear terms, can be expressed as

$$f_r = \frac{k_1}{\bar{k}} \sum_{i=1}^{3} \epsilon^i q_i + \epsilon^2 \frac{k_1}{\bar{k}} (1 - \delta) z_{l,2}^{\mathrm{nl}} + \epsilon^3$$
$$\left[\frac{(E^{(1)} A) \ell (j\pi)^4}{2\bar{k}} + \frac{k_3}{\bar{k}} + \frac{k_1}{\bar{k}} (1 - \delta) z_{l,3}^{\mathrm{nl}} \right] q_1^3 \tag{29}$$

Table 1 Coefficients of the asymptotic expansions of the nonlinear part of the hysteretic curvature

Branch	c_{1l}	c_{2l}	d_{1l}	d_{2l}	d_{3l}	d_{4l}	d_{5l}
1	$-\tfrac{1}{2}\bar{\gamma}$	$\tfrac{1}{2}(\bar{\gamma} - \bar{\beta})$	$-\bar{\gamma}$	$(\bar{\gamma} - \bar{\beta})$	$-\tfrac{1}{6}\bar{\gamma}\bar{\beta}$	$-\tfrac{1}{2}(\bar{\gamma} - \bar{\beta})\bar{\gamma}$	$\tfrac{1}{6}(\bar{\gamma} - \bar{\beta})^2$
2	$-\tfrac{1}{2}\bar{\gamma}$	$\tfrac{1}{2}(\bar{\gamma} + \bar{\beta})$	$-\bar{\gamma}$	$(\bar{\gamma} + \bar{\beta})$	$-\tfrac{1}{6}\bar{\gamma}\bar{\beta}$	$-\tfrac{1}{2}(\bar{\gamma} + \bar{\beta})\bar{\gamma}$	$\tfrac{1}{6}(\bar{\gamma} + \bar{\beta})^2$
3	$\tfrac{1}{2}\bar{\gamma}$	$-\tfrac{1}{2}(\bar{\gamma} - \bar{\beta})$	$\bar{\gamma}$	$-(\bar{\gamma} - \bar{\beta})$	$\tfrac{1}{6}\bar{\gamma}\bar{\beta}$	$-\tfrac{1}{2}(\bar{\gamma} - \bar{\beta})\bar{\gamma}$	$\tfrac{1}{6}(\bar{\gamma} - \bar{\beta})^2$
4	$\tfrac{1}{2}\bar{\gamma}$	$-\tfrac{1}{2}(\bar{\gamma} + \bar{\beta})$	$\bar{\gamma}$	$(\bar{\gamma} + \bar{\beta})$	$\tfrac{1}{6}\bar{\gamma}\bar{\beta}$	$-\tfrac{1}{2}(\bar{\gamma} + \bar{\beta})\bar{\gamma}$	$\tfrac{1}{6}(\bar{\gamma} + \bar{\beta})^2$

where

$$z_{l,2}^{nl} = \frac{k_{z2}}{k_1}(c_1\, q_{01}^2 + c_2\, q_1^2),$$

$$z_{l,3}^{nl} = \frac{k_{z2}}{k_1}\,(d_{1l}\, q_{01}\, q_{02} + d_{2l}\, q_1\, q_2) \tag{30}$$

$$+ \frac{k_{z3}}{k_1}\,(d_{3l}\, q_{01}^3 + d_{4l}\, q_{01}^2\, q_1 + d_{5l}\, q_1^3).$$

The coefficients reported in "Appendix" are computed for any jth mode. The values for the lowest mode are $k_1 = \bar{k} = \frac{E^{(1)}J}{\ell}\pi^4$, $k_3 = \bar{k}\frac{\pi^2}{4}$, $k_{z2} = -\frac{\bar{k}}{\ell}\frac{8\sqrt{2}}{3}$, $k_{z3} = \frac{\bar{k}}{\ell^2}\frac{3\pi^4}{2}$. Moreover, the damping force is expressed in discrete form as $f_d = 2\zeta\dot{q}$ and the excitation as $p = \mathcal{D}[\ddot{y}] = F\cos\Omega t$ with $F := |\ddot{y}|\int_0^1 \phi\, ds^*$ with $|\ddot{y}|$ indicating the amplitude of the assumed sinusoidal base acceleration $\ddot{y}$.

The reduced-order equation of motion for the lowest mode expressed up to third-order asymptotic terms thus becomes

$$\sum_{i=1}^{3}\epsilon^i[\ddot{q}_i + 2\zeta\dot{q}_i + q_i] + \epsilon^2(1-\delta)\,z_{l,2}^{nl}$$

$$+ \epsilon^3[\alpha q_1^3 + (1-\delta)z_{l,3}^{nl}] = \sum_{i=2}^{3}\epsilon^i F_i \cos\Omega t \tag{31}$$

where $\alpha = \frac{(E^{(1)}A)\,\ell^2}{2(E^{(1)}J)\pi^4} + \frac{\pi^2}{4}$.

Cantilever beams. The nondimensional form of the equation of motion (21) can be treated in the same way as for the hinged–hinged beams. Different definitions of the forces are obtained; that is,

$$f_i = \left\{\ddot{v}^*\left[1 - \tfrac{1}{2}(v^{*\prime})^2\right] + v^{*\prime}\int_0^s\left[v^{*\prime}\ddot{v}^{*\prime} + (\dot{v}^{*\prime})^2\right]ds\right.$$

$$- v^{*\prime\prime}\int_s^1\left[\int_0^s\left(v^{*\prime}\ddot{v}^{*\prime} + (\dot{v}^{*\prime})^2\right)d\xi\right]ds$$

$$\left. + v^{*\prime\prime}\int_s^1[\ddot{v}^*v^{*\prime}]d\xi\right\}, \tag{32a}$$

$$f_r = (M'' - v^{*\prime\prime}\int_s^1 v^{*\prime\prime}M'\,d\xi)/\bar{k}. \tag{32b}$$

The mode shapes of cantilever beams read

$$\phi_j(s^*) = \cos(\lambda_j s^*) - \cosh(\lambda_j s^*) - c_j\left[\sin(\lambda_j s^*)\right.$$
$$\left. - \sinh(\lambda_j s^*)\right]$$

where $c_j := (\cos\lambda_j + \cosh\lambda_j)/(\sin\lambda_j + \sinh\lambda_j)$. The frequencies are expressed as $\omega_j^2 = \lambda_j^4 E^{(1)}J/(\bar{k}\ell)$ with the roots for the lowest five modes given by

$\lambda_1 = 1.875$, $\lambda_2 = 4.694$, $\lambda_3 = 7.854$, $\lambda_4 = 10.995$, $\lambda_5 = 14.130$. We again assume $\omega_1 = 1$ so that $\bar{k} := \lambda_1^4 E^{(1)}J/\ell$.

The discretization of the restoring force, containing material and geometric nonlinearities, is treated next. The reduced-order form of the inertial terms is obtained as

$$f_i = \sum_{i=1}^{3}\epsilon^i\,\ddot{q}_i + \epsilon^3(m_1\, q_1^2\ddot{q}_1 + m_2\, q_1\,\dot{q}_1^2) \tag{33}$$

where $m_1 = (i_2 + i_3 + i_4 - \tfrac{1}{2}i_1)$ and $m_2 = i_2 + i_3$ with

$$i_1 := \mathcal{D}\left[\phi\,(\phi')^2\right], \quad i_2 := \mathcal{D}\left[\phi'\mathcal{I}_1(s)\right],$$

$$i_3 := \mathcal{D}\left[\phi''\mathcal{I}_2(s)\right], \quad i_4 := \mathcal{D}\left[\phi''\mathcal{I}_3(s)\right],$$

and the functions $\mathcal{I}_k(s)$ are defined in "Appendix". The generalized damping force and excitation have the same expressions as for the hinged–hinged beam. For the computation of the other nonlinear forces, besides the term $M''/(\ell\bar{k})$ already discussed, we show the treatment of $(v^*)''\int_s^1 (v^*)'' M_l'\,d\xi$. Discarding all terms in q of order greater than three, only the linear elastic contribution from the bending moment $\epsilon E^{(1)}J\kappa_1$ is retained, that is,

$$(v^*)''\int_s^1 (v^*)'' M_l'\,d\xi \approx E^{(1)}J(v^*)''\int_s^1 (v^*)''\kappa'\,d\xi$$

$$\approx \epsilon^3\frac{E^{(1)}J}{\ell}\left(\phi''\int_{s^*}^1 \phi''\phi'''\,d\xi\right)q_1^3.$$

In the contribution of the hysteretic part of the moment to the restoring force, $z_l^{nl} = \epsilon^2 z_{l,2}^{nl} + \epsilon^3 z_{l,3}^{nl}$, the quadratic and cubic terms are given by

$$z_{l,2}^{nl} = \frac{2\,s_{z2}}{\lambda_1^4\,\ell}\,(c_1\, q_{01}^2 + c_2\, q_1^2),$$

$$z_{l,3}^{nl} = \frac{2\,s_{z2}}{\lambda_1^4\,\ell}\,(d_{1l}\, q_{01}\, q_{02} + d_{2l}\, q_1\, q_2) + \frac{3\,s_{z3}}{\lambda_1^4\,\ell^2}\,(d_{3l}\, q_{01}^3$$

$$+ d_{4l}\, q_{01}^2\, q_1 + d_{5l}\, q_1^3)$$

where (s_{z2}, s_{z3}) are defined in "Appendix". The ensuing discrete form of the equation of motion can be conveniently written as

$$\sum_{i=1}^{3}\epsilon^i(\ddot{q}_i + 2\zeta\,\dot{q}_i + q_i) + \epsilon^2(1-\delta)z_{l,2}^{(nl)}$$

$$+ \epsilon^3(m_1\, q_1^2\ddot{q}_1 + m_2\, q_1\,\dot{q}_1^2) \tag{34}$$

$$+ \epsilon^3[\alpha\, q_1^3 + (1-\delta)z_{l,3}^{(nl)}] = \sum_{i=2}^{3}\epsilon^i F_i\,\cos\Omega t$$

where the ratio between the nonlinear and linear stiffness is $\alpha = \frac{s_3}{\lambda_1^4} = \frac{k_3}{k_1}$.

4 Asymptotic solutions via the method of multiple scales

Equation (34) is more general than Eq. (31) since it includes the inertia nonlinear terms. This is why we treat asymptotically Eq. (34) which is recast in state space form:

$$\sum_{i=1}^{3} \epsilon^i (\dot{q}_i - p_i) = 0,$$

$$\sum_{i=1}^{3} \epsilon^i (\dot{p}_i + 2\zeta\, p_i + q_i) + \epsilon^2 (1 - \delta) z_{l,2}^{(\mathrm{nl})}$$

$$+ \epsilon^3 (m_1\, q_1^2\, \dot{p}_1 + m_2\, q_1\, p_1^2)$$

$$+ \epsilon^3 [\alpha\, q_1^3 + (1 - \delta) z_{l,3}^{(\mathrm{nl})}] = \sum_{i=2}^{3} \epsilon^i F_i \cos \Omega\, t \quad (35a)$$

where (m_1, m_2) are nontrivial for cantilever beams, while $m_1 = 0 = m_2$ for hinged–hinged beams. By introducing the fast time scale t_0 and slow time scales $t_1 = \epsilon t$ and $t_2 = \epsilon^2 t$, the asymptotic terms of the generalized coordinate q_i, velocity p_i, and hysteretic force $z_{l,i}$ are assumed to depend on (t_0, t_1, t_2), namely,

$$q_i(t; \epsilon) = q_i(t_0, t_1, t_2), \quad p_i(t; \epsilon)$$
$$= p_i(t_0, t_1, t_2), \quad z_{l,i}(t; \epsilon) = z_{l,i}(t_0, t_1, t_2). \quad (35b)$$

The time derivatives are expressed as

$$\frac{\mathrm{d}}{\mathrm{d}t}(\cdot) = \partial_0(\cdot) + \epsilon \partial_1(\cdot) + \epsilon^2 \partial_2(\cdot) \quad (35c)$$

where $\partial_{i-1}(\cdot) := \partial(\cdot)/\partial t_{i-1}$. We also scale the damping term as $\zeta \to \epsilon \zeta$, the excitation term as a second-order term (i.e., $F_3 = 0$), and further express the frequency detuning from resonance as $\Omega = 1 + \epsilon \sigma$. This asymptotic scaling is tuned to tackle the primary resonance condition of the lowest bending mode away from internal resonance conditions. Since the quadratic piece-wise hysteretic terms imply a solvability condition at second order, the excitation and damping forces are scaled so as to appear at this order.

Therefore, substituting Eqs. (35b) and (35c) into (35a), the following hierarchy of problems is obtained: order ϵ:

$$\partial_0 q_1 - p_1 = 0,$$
$$\partial_0 p_1 + q_1 = 0 \quad (36)$$

order ϵ^2:

$$\partial_0 q_2 - p_2 = -\partial_1 q_1,$$
$$\partial_0 p_2 + q_2 = -\partial_1 p_1 - 2\zeta\, p_1 \quad (37)$$
$$- (1 - \delta) z_{l,2} + F \cos(t_0 + \sigma t_1)$$

order ϵ^3:

$$\partial_0 q_3 - p_3 = -\partial_1 q_2 - \partial_2 q_1,$$
$$\partial_0 p_3 + q_3 = -\partial_1 p_2 - \partial_2 p_1 - 2\zeta\, p_2 - (1 - \delta) z_{l,3}$$
$$- \alpha\, q_1^3 - m_1 q_1^2 \partial_0 p_1 - m_2 q_1 p_1^2. \quad (38)$$

First-order problem. The solution of the first-order problem (36) can be expressed as

$$q_1 = a(t_1, t_2) \cos(t_0 + \vartheta(t_1, t_2)),$$
$$p_1 = -a(t_1, t_2) \sin(t_0 + \vartheta(t_1, t_2)). \quad (39)$$

The first-order solution reaches its maximum when $p_1 = 0$ at $\tau_0 = -\vartheta(t_1, t_2)$. Moreover, the instant of time when the displacement goes through zero is $\tau_1 = \tau_0 + \pi/2$, the instant when the velocity is zero again (reaches the maximum displacement in the negative direction) is $\tau_2 = \tau_0 + \pi$; the instant when it passes through zero again is $\tau_3 = \tau_0 + 3\pi/2$ and finally the solution reaches the maximum again after one period, namely, at $\tau_4 = \tau_0 + 2\pi$. These instants of time have the meaning of branch-to-branch switching times so the solution for the lth branch is defined for $t_0 \in [\tau_{l-1}, \tau_l]$.

Second-order problem. Substituting the first-order solution (39) into the second-order problem (37) yields the inhomogeneous terms given in piece-wise fashion as

$$\mathbf{r}_{2,l} = \begin{bmatrix} -\partial_1 q_1 \\ -\partial_1 p_1 - 2\zeta\, p_1 - (1 - \delta) z_{l,2} + F \cos(t_0 + \sigma t_1) \end{bmatrix}.$$

An alternative way to express the right-hand side over one period is to make use of the Heaviside functions, namely, $\mathbf{r}_2 = \sum_{l=1}^{4} \mathbf{r}_{2,l}[H(t_0 - \tau_{l-1}) - H(t_0 - \tau_l)]$. The problem is made solvable imposing the following two solvability conditions:

$$\int_{\tau_0}^{\tau_0+2\pi} \mathbf{w}_j^\top \mathbf{r}_2 \mathrm{d}t_0 = \sum_{l=1}^{4} \int_{\tau_{l-1}}^{\tau_l} \mathbf{w}_j^\top \mathbf{r}_{2,l} \mathrm{d}t_0 = 0, \quad j = 1, 2$$

with $\mathbf{w}_1 = [\sin t_0, \ \cos t_0]^\top$ and $\mathbf{w}_2 = [\cos t_0, \ -\sin t_0]^\top$ being the solutions of the adjoint homogeneous problem. The following modulation equations are obtained:

$$\partial_1 a = -\zeta a - \frac{2\,\bar{\beta}(1-\delta)\,k_{z2}\,a^2}{3\pi}$$
$$+ \frac{F}{2} \sin(t_1\,\sigma_1 - \vartheta),$$
$$\partial_1 \vartheta = -\frac{2\,\bar{\gamma}(1-\delta)\,k_{z2}\,a}{3\pi} + \frac{F}{2a} \cos(t_1\,\sigma_1 - \vartheta). \quad (40)$$

These solvability conditions are inserted into the second-order problem which is then solved for $q_{2,l}$ and $p_{2,l}$. The ensuing piece-wise solutions are determined within 4×2 integration constants. The continuity conditions are imposed on the obtained expressions as

$$q_{2,l}(\tau_l) = q_{2,l+1}(\tau_l),$$
$$p_{2,l}(\tau_l) = p_{2,l+1}(\tau_l), \quad \text{for } l = 1, 2, 3$$

which yield six of the eight constants. The remaining two coefficients are obtained by enforcing the following orthogonality conditions:

$$\sum_{l=1}^{4} \int_{\tau_{l-1}}^{\tau_l} \mathbf{w}_1^\top \begin{bmatrix} q_{2,l} \\ p_{2,l} \end{bmatrix} \mathrm{d}t_0 = 0,$$
$$\sum_{l=1}^{4} \int_{\tau_{l-1}}^{\tau_l} \mathbf{w}_2^\top \begin{bmatrix} q_{2,l} \\ p_{2,l} \end{bmatrix} \mathrm{d}t_0 = 0.$$

The second-order solution can be also expressed for the time duration of the excitation period (i.e., $t_0 \in [\tau_0, \tau_0 + 2\pi]$) as before making use of the Heaviside functions to obtain

$$q_2 = \sum_{l=1}^{4} q_{2,l}[H(t_0 - \tau_{l-1}) - H(t_0 - \tau_l)],$$
$$p_2 = \sum_{l=1}^{4} p_{2,l}[H(t_0 - \tau_{l-1}) - H(t_0 - \tau_l)]. \quad (41)$$

Third-order problem Substituting the second-order solution (41) into the third-order problem (38) and making use of the modulation equations at second order yield the following right-hand side:

$$\mathbf{r}_{3,l} = -\begin{bmatrix} \partial_1 q_2 \partial_2 q_1 \\ h_{3,l} + (1-\delta)z_{l,3} + \alpha\,q_1^3 \end{bmatrix}$$

with $h_{3,l} = \partial_1 p_2 + \partial_2 p_1 + 2\zeta\,p_2 + m_1 q_1^2 \partial_0 p_1 + m_2 q_1 p_1^2$

To make the problem solvable, we enforce again the solvability conditions

$$\sum_{l=1}^{4} \int_{\tau_{l-1}}^{\tau_l} \mathbf{w}_1^\top \mathbf{r}_{3,l} \, \mathrm{d}t_0 = 0, \quad \sum_{l=1}^{4} \int_{\tau_{l-1}}^{\tau_l} \mathbf{w}_2^\top \mathbf{r}_{3,l} \, \mathrm{d}t_0 = 0$$

thus obtaining the modulation equations in $(\partial_2 a, \ \partial_2 \vartheta)$.

Note that all terms with derivatives greater than one in both t_1 and t_2 are dropped since they are of order greater than two in the modulation equations.

Modulation equations. According to the method of reconstitution, the modulation equations at third order are combined with the modulation equations at second order to obtain

$$\dot{a} = \epsilon\,\partial_1 a + \epsilon^2\,\partial_2 a, \quad \dot{\vartheta} = \epsilon\,\partial_1 \vartheta + \epsilon^2\,\partial_2 \vartheta. \quad (42)$$

Moreover, we substitute $\psi = \sigma t_1 - \vartheta$ and make use of the detuning condition $\Omega = 1 + \epsilon\,\sigma$, so that

$$\dot{\psi} = \epsilon(\sigma - \partial_1 \vartheta) - \epsilon^2\,\partial_2 \vartheta \equiv \sigma - \dot{\vartheta}.$$

The reconstituted modulation equations become

$$\dot{a} = -\zeta a + f\left(\tfrac{1}{2} - a\,g_s\right) \sin\psi$$
$$+ f\left(\tfrac{\zeta}{4} - a\,g_c\right) \cos\psi - g_{a2}\,a^2 - g_{a3}\,a^3,$$
$$a\dot{\psi} = -f\left(\tfrac{\zeta}{4} - a\,h_s\right) \sin\psi$$
$$+ f\left(\tfrac{1}{2} + a\,h_c\right) \cos\psi - (1 - \Omega - \tfrac{1}{2}\zeta^2)\,a$$
$$+ h_{a2}\,a^2 - h_{a3}\,a^3$$
$$(43)$$

with

$$g_s = k_{z2}(1-\delta)\frac{\bar{\beta}}{6\pi}, \quad g_c = k_{z2}(1-\delta)\frac{\bar{\gamma}}{3\pi},$$
$$h_c = k_{z2}(1-\delta)\frac{\bar{\beta}}{3\pi},$$
$$g_{a2} = k_{z2}(1-\delta)\frac{2\bar{\gamma}}{3\pi},$$
$$g_{a3} = k_{z2}^2(1-\delta)^2(3\pi-4)\frac{\bar{\gamma}\bar{\beta}}{9\pi^2},$$
$$h_s = k_{z2}(1-\delta)\frac{\bar{\gamma}}{6\pi},$$
$$h_{a2} = k_{z2}(1-\delta)\frac{2\bar{\beta}}{3\pi},$$

$$h_{a3} = \frac{1}{432\pi^2} k_{z2}^2 (1-\delta)^2 [(256 - 45\pi^2)\bar{\beta}^2$$
$$- (512 - 63\pi^2)\bar{\gamma}^2]$$
$$+ \alpha\frac{3}{8} - k_{z3}(1-\delta)\frac{1}{16}(3\,\bar{\gamma}^2 - \bar{\beta}^2)$$
$$+ \frac{1}{8}(m_2 - 3\,m_1). \tag{44}$$

Frequency response and bifurcations. The implicit form of the frequency response function is obtained solving (43) for $(\sin\psi,\ \cos\psi)$ and making use of the fundamental trigonometric identity $\sin^2\psi + \cos^2\psi = 1$. The result for the implicit form is

$$\mathcal{G}(\Omega,\,a) = \mathcal{G}_1(a)\,\Omega^2 + \mathcal{G}_2(a)\,\Omega$$
$$+ \mathcal{G}_3(a) - \mathcal{G}_f(a)\,F^2 = 0, \tag{45}$$

whereas the explicit form can be obtained solving the above equation in Ω:

$$\Omega = -\frac{\mathcal{G}_2(a)}{2\,\mathcal{G}_1(a)} \pm \frac{\sqrt{(\mathcal{G}_2(a))^2 - 4\mathcal{G}_1(a)(\mathcal{G}_3(a) - \mathcal{G}_f(a)\,F^2)}}{2\,\mathcal{G}_1(a)}. \tag{46}$$

The coefficients $\mathcal{G}_k$ are omitted for their lengthy expressions. The backbone curves determined as the loci of the peaks of the frequency response curves are given by

$$\Omega = -\frac{\mathcal{G}_2(a)}{2\,\mathcal{G}_1(a)}. \tag{47}$$

A qualitative switch of behavior is observed in general nonlinear oscillators when the backbone curve exhibits a wiggle due to a change of bending of the curve which entails that the frequency response turns from being hardening to softening or vice versa. The above transitions occur at threshold amplitudes where the local change of frequency with respect to the oscillation amplitude vanishes, that is, $\frac{d\Omega}{da} = 0$. This entails a linear response of the oscillator to within the sought order of approximation. Such amplitudes a_{S} are found as roots of the following equation:

$$(\mathcal{G}_1\,\partial_a\mathcal{G}_2 - \mathcal{G}_2\,\partial_a\mathcal{G}_1)\Big|_{a_{\mathrm{S}}} = 0 \tag{48}$$

We will refer to these points as *nonlinearity switching points*.

On the other hand, the stability of the periodic solutions is dictated by the eigenvalues of the modulation equations. It is known that a loss of stability

occurs along the frequency response curves at the so-called fold bifurcation points where vertical tangency is attained. In other words, $\frac{d\Omega}{da} = 0$ computed for the frequency response function. This condition can be obtained as $\partial_a\mathcal{G}(\Omega,\,a) = 0$ which yields the loci of the fold bifurcation points in the form:

$$\mathcal{C}(\Omega,\,a)\ = \Omega + \frac{\partial_a\mathcal{G}_2}{2\,\partial_a\mathcal{G}_1}$$
$$\mp \frac{\sqrt{(\partial_a\mathcal{G}_2)^2 - 4\partial_a\mathcal{G}_1(\partial_a\mathcal{G}_3 - \partial_a\mathcal{G}_f\,F^2)}}{2\,\partial_a\mathcal{G}_1} = 0. \tag{49}$$

The two fold lines obtained using Eq. (49) coalesce into a point (codimension-two fold point) at a given driving excitation amplitude and frequency and disappear thereafter upon changes of the frequency/amplitude. The loci of these bifurcation points have a special meaning for the system dynamics as they represent the boundary between regions of globally stable responses and regions of multi-stable responses.

5 Asymptotic results

In this section, we discuss the main results obtained in terms of backbone curves, frequency response curves, and behavior charts considering the primary resonance of the lowest mode (i.e., choosing the mode with $j = 1$ in (24) and subsequent equations). The behavior charts depict softening/hardening regions in the space of the constitutive parameters and excitation amplitude/frequency. The softening versus hardening regions depend on the choice of material parameters such as those regulating the CNT–polymer interfacial constitutive properties, the CNT volume fraction, etc. The computations were carried out considering the physical parameters of the nanocomposite beams which were experimentally tested and characterized in [12] with span $\ell = 34.5 \times 10^{-3}$ m, width $b = 9.78 \times 10^{-3}$ m, thickness $h = 0.79 \times 10^{-3}$ m, PBT polymer Young's modulus $E_{\mathrm{m}} = 2.1$ GPa, Poisson's ratio $\nu_{\mathrm{m}} = 0.39$, mass density $\rho_{\mathrm{m}} = 1,310$ kg/m^3, CNT Young's modulus $E_{\mathrm{c}} = 970$ GPa, CNT Poisson's ratio $\nu_{\mathrm{c}} = 0.1$, mass density $\rho_{\mathrm{c}} = 1,750$ kg/m^3. Moreover, the damping ratio was set to $\zeta = 1.85\%$, the baseline CNT %wt was 2% (i.e., volume fraction $\phi_{\mathrm{c}} = 1.505\%$). The corresponding nondimensional parameters are: $\bar{k} = 21.259$, $\delta = 0.672637$, $\alpha = 122.407$,
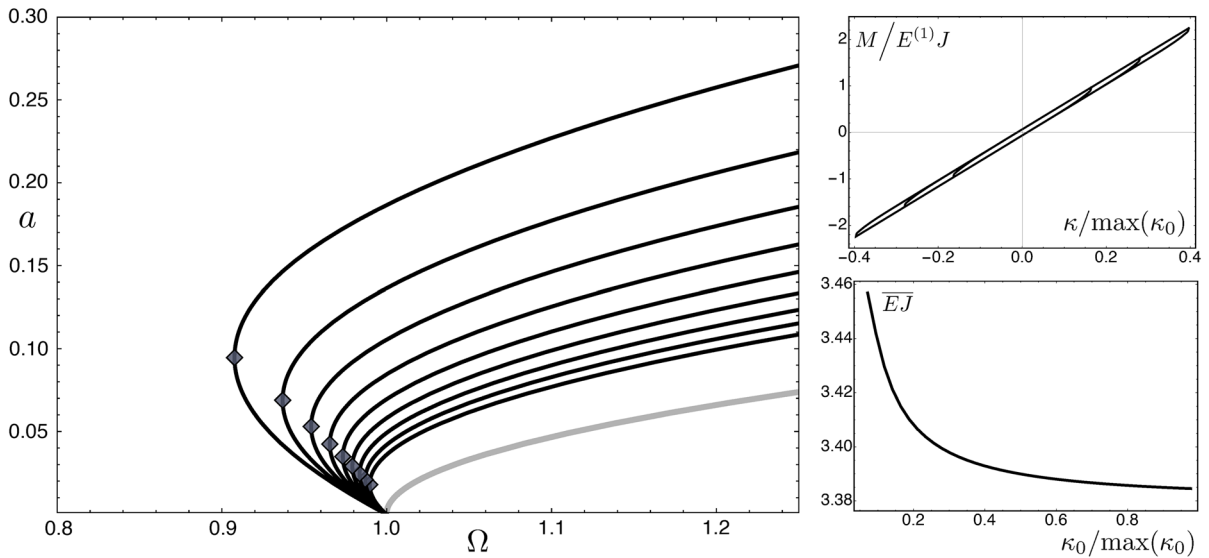
Fig. 4 (left) Backbone curves of the lowest mode of hinged–hinged nanocomposite beams with $n = 1$, $(\bar{\gamma}, -\bar{\beta}) = [(5.2, 4.7),$ $(5.6, 5.1), (6.0, 5.5), (6.4, 5.9), (6.8, 6.3), (7.2, 6.7), (7.6, 7.1),$ $(8.0, 7.5), (8.4, 7.9)] \times 10$. The backbone curve of the beam with-

out hysteresis is represented by the gray line. (top right) Moment–curvature hysteresis cycles and (bottom right) average bending stiffness $\overline{EJ}$ versus curvature amplitude

$k_{z2} = -0.343411$, $k_{z3} = 0.122759$ for hinged–hinged beams; $\bar{k} = 2.69802$, $\delta = 0.672637$, $\alpha = 1.11737$, $m_1 = 2.44287$, $m_2 = 4.59677$, $k_{z2} = -0.301221$, $k_{z3} = 0.0697131$ for cantilever beams. The results are presented first for hinged–hinged beams followed by the results obtained for the cantilevers.

Hinged–hinged beams. A sequence of backbone curves given by Eq. (47) corresponding to various parameters $(\bar{\beta}, \bar{\gamma})$ is shown in Fig. 4. In particular, such curves are obtained varying $\bar{\beta}$ in the range $[-1, 1] \times 10^3$ and $\bar{\gamma}$ as $\bar{\gamma} = 1/z_{max} - \bar{\beta}$, with the aim to prescribe a constant maximum value $z_{max} = 0.2$ for the hysteretic (nondimensional) displacement. The curves show a softening nonlinearity until reaching the threshold amplitude a_S represented by the black diamonds where a change from softening to hardening occurs. Such change is explained by the fact that at low amplitudes the softening hysteretic frictional CNT–polymer sliding embedded in the moment–curvature relationship dominates the cubic stretching-induced hardening which, conversely, becomes dominant at larger oscillation amplitudes. The softening feature of hysteresis is confirmed by the decreasing trend of the average bending stiffness in Fig. 4 (bottom right). Therefore, the nanocomposite beam with suitably tuned interfacial CNT/polymer
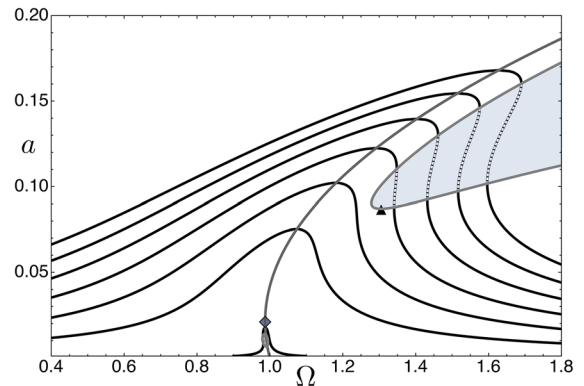

Fig. 5 Frequency response curves of the lowest mode of hinged–hinged nanocomposite beams with $n = 1$, $(\bar{\gamma}, -\bar{\beta}) = (5.6, 5.1) \times 10$, and $F = [0.02, \ldots, 8] \times 10^{-2}$

properties can undergo a qualitative change in its nonlinear dynamic flexural behavior with respect to the baseline linearly elastic hinged–hinged beam which, without hysteresis, exhibits a hardening response (see gray line in Fig. 4).

A family of frequency response curves obtained for $(\bar{\gamma}, -\bar{\beta}) = (5.6, 5.1) \times 10$ is shown in Fig. 5 together with the shaded unstable regions bounded by the loci of fold bifurcation points [i.e., solutions of Eq. (49)]
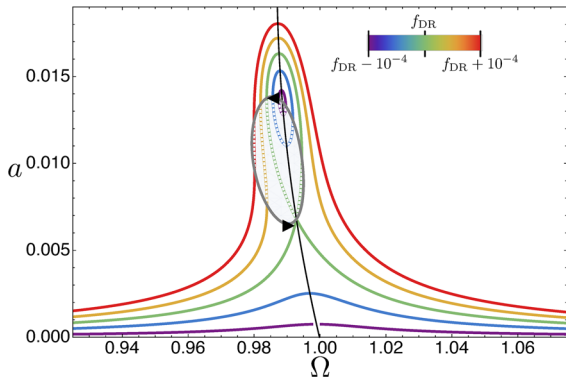
Fig. 6 A zoom of the frequency response curves in Fig. 5 exhibiting the DRC obtained for F in the range $F = [F_{DR} - 10^{-4}, \ldots, F_{DR} + 10^{-4}]$

indicated by the solid gray lines. Along the softening branch of the backbone we observe a closed region bounded by gray lines which signals the existence of unstable branches on both sides of the backbone.

A close analysis of the solutions in that region reveals the existence of detached resonance curves (DRC). Detached resonance curves have been widely investigated both theoretically and experimentally in a variety of nonlinear oscillators [45–48]. Recently, a spectral submanifold theory was proposed to provide analytic predictions of the periodic responses including isolated forced responses belonging to detached resonance curves [49, 50].

The occurrence of DRC can be detected as the condition for which the implicit form of the FRC given by Eq. (45) satisfies the following two equations and two inequalities [45]:

$$\frac{\partial \mathcal{G}}{\partial a} = 0 \text{ and } \frac{\partial \mathcal{G}}{\partial \Omega} = 0, \text{ with } \det \mathbf{H} > 0 \text{ and } \frac{\partial^2 \mathcal{G}}{\partial a^2} \neq 0 \tag{50}$$

with $\mathbf{H}$ being the Hessian of $\mathcal{G}$. On the other hand, the coalescence of the DRC with the main resonance curve occurs when the same above equations hold but with $\det \mathbf{H} < 0$ [45].

To find the above critical conditions, we substitute the explicit form of the FRF given by Eq. (46) into Eq. (50) which yields two equations in (a, F) whose solution is $a_{DR} = 6.7947 \times 10^{-3}$ and $F_{DR} = 1.2612 \times 10^{-4}$. In turn, Eq. (46) provides the associated critical frequency $\Omega_{DR} = 0.99283$. By letting (a_B, F_B) denote the

solution of the bifurcation condition for the coalescence of the DRC with the main resonance curve, the DRC is predicted to exist in the excitation amplitude range $F_{DR} < F < F_B$.

The evolution of the DRCs is portrayed in Fig. 6. For $F < F_{DR}$, the frequency response curves are softening, single-valued and stable. At $F = F_{DR}$, a DRC is born as an isola (see purple line in Fig. 6) and grows with increasing F up to the critical force $F = F_B$ where the DRC and the main resonance curve coalesce. Upon further force increases, the DRC disappears (see green line in Fig. 6). Above F_B, the entire (single) resonance curve has two regions of unstable solutions one of which (the right branch) becomes stable past the condition in which the resonance curve touches tangentially the right fold line. Moreover, for increasing F the left unstable branch gets smaller until becoming a singular point when the resonance curve touches tangentially the left fold line. The associated excitation level is denoted by F_{F1}. For $F > F_{F1}$, the softening resonance curve becomes single-valued and stable. Upon further increasing the amplitude, the resonance curves show a wiggle due to the change of nonlinearity from softening to hardening at a_S. The force F such that the corresponding FRC has its peak corresponding to a_S is denoted by F_S. Thus, for $F > F_S$, the FRCs become hardening, single-valued and stable until touching the codimension-two fold bifurcation point where the two fold lines coalesce at F_{F2}. Past F_{F2}, the hardening FRCs become multi-valued and multi-stable with an unstable branch and two stable branches.

A closer understanding of the wiggling of the backbones and associated FRFs can be gained observing in Fig. 7 the evolution of the restoring force–deflection hysteresis cycles corresponding to the periodic solutions. The hysteresis loops are obtained substituting the second-order periodic solution into the expansion of the restoring force up to cubic terms. As shown in Fig. 7, notwithstanding the fact that the cycles obtained along the low-amplitude branch of the backbone show a thin hysteresis, such softening hysteresis confers a softening character to the response because the beam stretching nonlinearity is not activated at such small amplitudes. On the other hand, at larger amplitudes the geometric stretching nonlinearity changes the hysteresis cycles making them hardening due to a clear increase of stiffness at higher amplitudes.

The overall nonlinear dynamic behavior of the investigated hinged–hinged nanocomposite beams can be

Fig. 7 a, b, c
Force–deflection curves and
(bottom) frequency
response curves of the
lowest mode of
nanocomposite
hinged–hinged beams when
$n = 1$,
$(\bar{\gamma}, -\bar{\beta}) = (5.6, 5.1) \times 10$
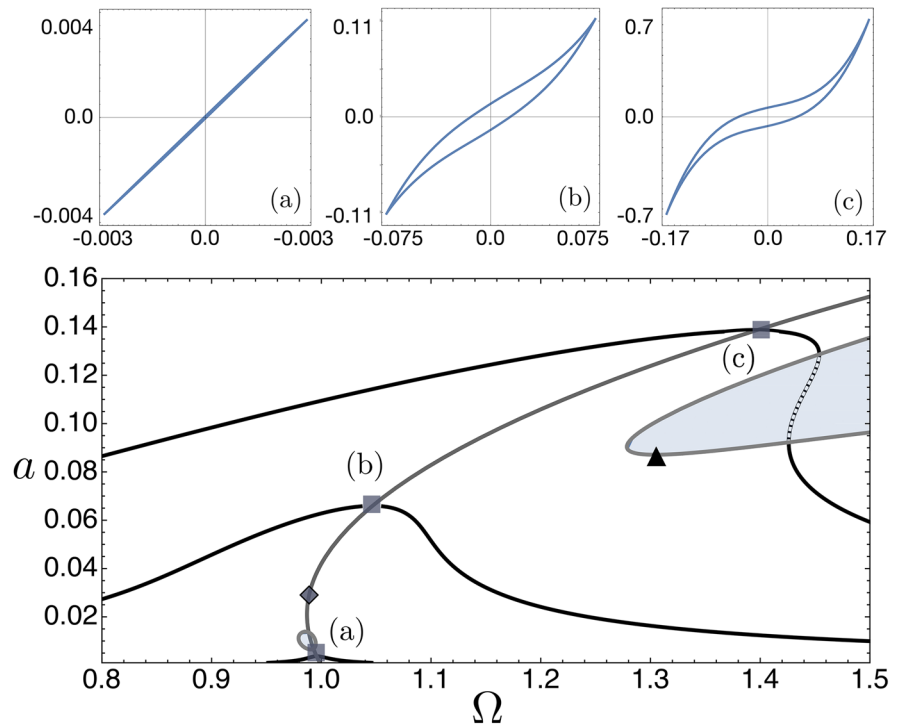
better pictured using the so-called *behavior charts* constructed in the space of the constitutive parameters and excitation amplitudes (i.e., charts exhibiting regions of different behavior bounded by curves obtained as loci of bifurcation points and nonlinearity switching points). An interesting behavior can be obtained via continuation of the nonlinearity switching points together with continuation of the codimension-two fold points in the plane (F, β). The first curve separates regions of softening and hardening behavior. The second curve separates regions of single-valued and stable responses from regions of multi-valued and multi-stable responses. One of such examples is shown in Figs. 8 and 9 where the shaded region indicates hardening responses, while the white region denotes softening responses. Moreover, the shaded light blue region is the multi-valued, multi-stable region separated through the black line from the region below of single-valued, stable responses. Figure 9 is a zoom of Fig. 8 restricted to the range of lower excitation amplitudes where we observe the existence of two curves obtained as loci of codimension-two fold points denoted by left-pointing triangles (coalescence of the two left fold lines in Fig. 6) and right-pointing triangles (coalescence of the two right fold lines in Fig. 6). These curves, in turn, coa-
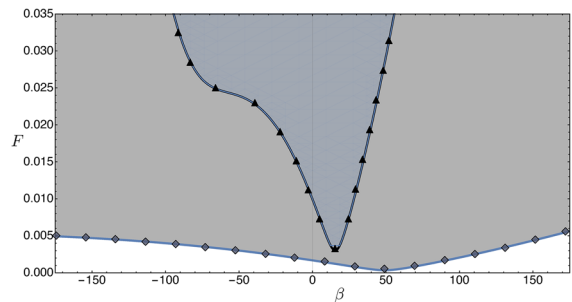

Fig. 8 Behavior chart of the lowest mode of hinged–hinged beams obtained with the starting values of the parameters employed in Fig. 5. The black solid curve is the continuation of the codimension-two fold points (black up-pointing triangles) and the blue solid line indicates the loci of the nonlinearity switching points (filled black diamonds)

lesce at $a_{DR} = 6.7947 \times 10^{-3}$ and $F_{DR} = 1.2612 \times 10^{-4}$ (onset of DRC) for the same constitutive parameter values used in Fig. 6. In the region between the two lines, the softening responses are multi-valued and multi-stable with the coexistence of DRC (only within a sub-region between the two lines decorated with left- and right-pointing triangles).

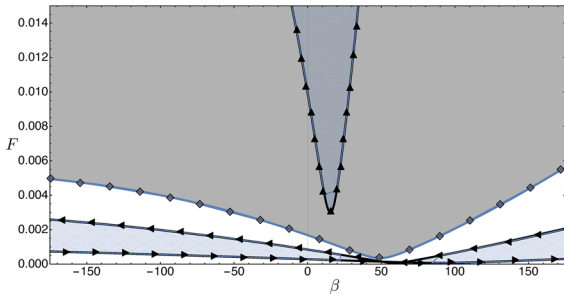*Hinged–hinged versus cantilever beams*. It is of theoretical and technical interest to compare the nonlinear

Fig. 9 A zoom of the behavior chart in Fig. 8. The black solid curve is the continuation of the codimension-two fold points (black up-triangles) and the blue solid line indicates the loci of the nonlinearity switching points (filled blue dots). The black left-pointing triangles and right-pointing triangles indicate the continuation of the left and right codimension-two fold points corresponding to the DRC

Fig. 10 Backbone curves of the lowest mode of nanocomposite hinged–hinged and cantilever beams. The constitutive parameters are: $n = 1$, $(\bar{\gamma}, -\bar{\beta}) = [(5.2, 4.7), (5.6, 5.0), (6.0, 5.5), (6.4, 5.9), (6.8, 6.3), (7.2, 6.7), (7.6, 7.1), (8.0, 7.5), (8.4, 7.9), (8.8, 8.3)] \times 10$. The dashed (solid) line indicates cantilever (hinged–hinged) beams. The backbone curves of the elastic beams (without hysteresis) are indicated by the gray lines

behaviors of axially restrained beams (hinged–hinged) against the behavior of axially unrestrained beams (cantilevers). These two kinds of beams are often employed as archetypal components in the design of structures across various scales. Just to mention a few, cantilever beams are employed as micromass [2] or bio-chemical sensors due to their greater flexibility. The comparison is here carried out using only the backbone curves computed for the nanocomposite beams and for the beams without hysteresis (i.e., beams made of pure polymer). Elastic cantilever beams are known to be mildly hardening in the lowest mode and softening in the higher modes (see dashed gray line in Fig. 10). The addition of nanostructural hysteresis introduces the softening characteristic nonlinearity (i.e., the backbone curves are bent to the left). Conversely, elastic hinged–hinged beams are strongly hardening due to the stretching contribution whereas the introduction of CNT/polymer hysteresis turns them into softening at low amplitudes albeit they maintain the hardening characteristic at large amplitudes. Note that the slope of the hardening backbones does not change since it is dominated by the geometric stretching nonlinearity which is independent from the nonlinear constitutive parameters.

Finally, to investigate all features of the cantilever beams, the backbone curve and the frequency response curves of the cantilevers are shown in Fig. 11 where two regions of multi-stable responses are present. While this trend has a clear theoretical interest, the underlying constitutive behavior is being experimentally proved in the investigated nanocomposites.
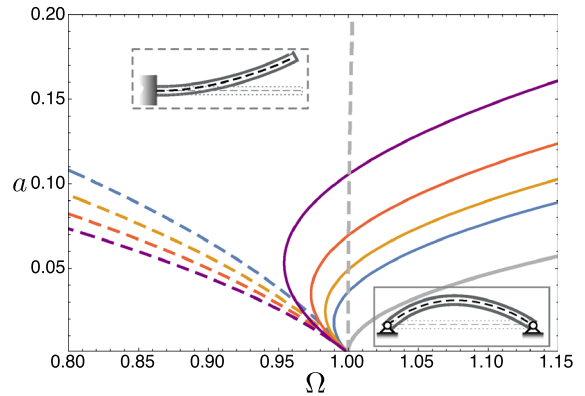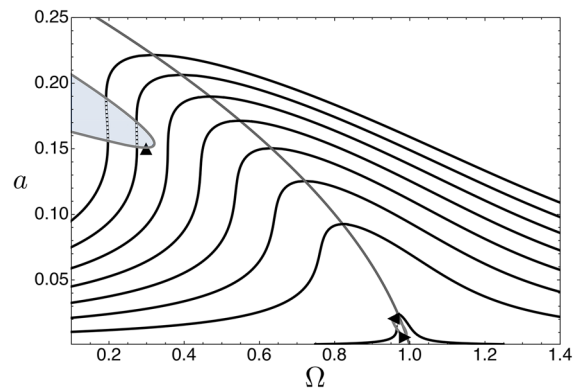

Fig. 11 (left) Backbone curve and frequency response curves of the lowest mode of nanocomposite cantilevers. The constitutive parameters are: $n = 1$, $(\bar{\gamma}, -\bar{\beta}) = (5.6, 5.1) \times 10$

6 Conclusions

This work proposed an original asymptotic modeling approach and analysis tailored for carbon nanotube nanocomposite beams with different boundary conditions. A nonlinear 3D nanocomposite constitutive model capable of capturing the hysteretic nanostructural stick-slip behavior between the CNTs and the hosting polymer matrix was reduced to accommodate the Saint-Venant plane bending kinematic state parametrized by two generalized strains (i.e., the elongation of the centerline and the bending curvature). The tension–elongation and moment–curvature relation-

ships were obtained according to an unusual derivation by which the tangent conditions in the CNT/polymer stick phase at the origin and past the onset of CNT slip were obtained employing the 1D-reduced constitutive model. The transition between these two states (namely, elastic and post-elastic phases) was assumed to be regulated by a hysteresis operator that mimics the Bouc–Wen model. Two nonlinear mechanical models were thus constructed, both featuring unshearability, one valid for (axially restrained) extensible beams and the other for (axially unrestrained) inextensible beams.

The discretization of the underlying infinite-dimensional systems incorporating hysteresis in the constitutive relationships was another challenge. To this end, the moment–curvature relationship in rate form was integrated to yield a piece-wise closed-form representation for each of the four branches of the hysteresis cycles. The obtained piece-wise closed-form moment–curvature relationship was expanded in Taylor series and treated asymptotically in the context of the one-mode Galerkin discretization of the deflection field. The resulting piece-wise reduced-order nanocomposite beam model was specialized for hinged–hinged and cantilever beams. The ensuing piece-wise ODEs were thus treated by the method of multiple scales to obtain the periodic responses to harmonic base excitations together with the frequency response functions.

The families of frequency response curves and behavior charts were unfolded by spanning suitable ranges of the constitutive parameters and excitation driving the primary resonance of the fundamental mode. The results showed how the interplay between the CNT/polymer nanostructural hysteretic nonlinearity and the geometric/inertia nonlinearities gives rise to rich and unexpected nonlinear behaviors. The constitutive nonlinearity of the nanocomposites was shown to be responsible for a remarkable tunability of the nonlinear frequency (softening versus hardening) and multistability (single-valued, stable responses versus multi-valued, multistable responses).

Appendix

Derivation of the equations of motion for nonlinear, nanocomposite beams. Consider the fixed reference frame $(O, \mathbf{e}_1, \mathbf{e}_2, \mathbf{e}_3)$ in Fig. 3 and the restricted plane of motion described by $(O, \mathbf{e}_3, \mathbf{e}_1)$. Let s denote the material coordinate that spans the beam base line in the reference configuration. The local frame $\{\mathbf{b}_1, \mathbf{b}_2, \mathbf{b}_3\}$ with $(\mathbf{b}_1, \mathbf{b}_2)$ describing the orientation of the material cross sections is given by $\mathbf{b}_1 = -\sin\theta\mathbf{e}_3 + \cos\theta\mathbf{e}_1$, $\mathbf{b}_3 = \cos\theta\mathbf{e}_3 + \sin\theta\mathbf{e}_1$ where θ denotes the counterclockwise angle by which the cross section at s is flexurally rotated about $\mathbf{b}_2 = \mathbf{e}_2$. The current position of the base point of the cross section is described by $\mathbf{r}(s, t) = s\mathbf{e}_3 + y(t)\mathbf{e}_1 + \mathbf{u}(s, t)$ where the displacement vector relative to the moving frame is $\mathbf{u}(s, t) = u(s, t)\mathbf{e}_3 + v(s, t)\mathbf{e}_1$ and $y(t)\mathbf{e}_1$ is the prescribed base excitation. The generalized strains are expressed as $\boldsymbol{\nu}(s, t) = \nu\mathbf{b}_3 + \eta\mathbf{b}_1$ where $\nu = \partial_s\mathbf{r}\cdot\mathbf{b}_3$ is the beam stretch, $\eta = \partial_s\mathbf{r}\cdot\mathbf{b}_1$ the shear strain, and ∂_s denotes differentiation with respect to the material coordinate. Moreover, $\kappa = \partial_s\theta$ (i.e., the spatial rate of change of θ) describes the bending curvature.

By letting $\mathbf{n}$ and $\mathbf{m}$ denote the beam contact force and couple (i.e., generalized stress resultants), the equations of motions are obtained enforcing the balance of linear and angular momentum [11]

$$\partial_s\mathbf{n} + \mathbf{f} = \rho A\partial_{tt}\mathbf{r} + \rho I\,\partial_{tt}\mathbf{b}_1, \tag{51}$$

$$\partial_s\mathbf{m} + (\boldsymbol{\nu} \times \mathbf{n})\cdot\mathbf{e}_2 + \mathbf{c}$$
$$= [\mathbf{b}_1 \times (\rho I\,\partial_{tt}\mathbf{r} + \rho J\,\partial_{tt}\mathbf{b}_1)]\cdot\mathbf{e}_2 \tag{52}$$

where ∂_t indicates differentiation with respect to time. The contact force $\mathbf{n}$ and contact couple $\mathbf{m}$ are expressed in the local frame as $\mathbf{n} = Q\mathbf{b}_1 + N\mathbf{b}_3$, $\mathbf{m} = M\mathbf{b}_2$ where Q denotes the shear force, N the tension and M the bending moment. Moreover, ρI is the first mass moment of the cross section about $\mathbf{b}_2$ and ρJ is the mass moment of inertia. The external force in the fixed frame is expressed as $\mathbf{f} = f\,\mathbf{e}_1$. The first moment ρI vanishes if the base line is chosen to coincide with the

beam centerline. Moreover, the local frame $(\mathbf{b_1}, \mathbf{b_2})$ is further assumed to be collinear with the principal axes of inertia of the cross section. In component form, the equations of motion can be written as

$$\partial_s N - \kappa Q + \mathbf{f} \cdot \mathbf{b}_3 = \rho A [\partial_{tt} u \, \mathbf{e}_3 \\ + (\partial_{tt} y + \partial_{tt} v) \, \mathbf{e}_1] \cdot \mathbf{b}_3, \quad (53)$$

$$\partial_s Q + \kappa N + \mathbf{f} \cdot \mathbf{b}_1 = \rho A [\partial_{tt} u \, \mathbf{e}_3 \\ + (\partial_{tt} y + \partial_{tt} v) \, \mathbf{e}_1] \cdot \mathbf{b}_1, \quad (54)$$

$$\partial_s M + \nu Q - \eta N + c = \rho J \partial_{tt} \theta. \quad (55)$$

For unshearable beams, the shear force Q is computed using Eq. (55) and substituted into Eq. (54). The constitutive equations are presented next in the context of the two unshearable (extensible and inextensible) beam models.

Extensible beams. Axially restrained beams are subject to stretching induced by the transverse motion. These beams are often modeled according to the Mettler theory which is based on *ad hoc* kinematic and mechanical assumptions [11]. Here the equations are deduced directly from the geometrically exact equations of motion for unshearable beams and the main steps are summarized in order to show how the model incorporating the hysteretic constitutive nonlinearity is forged.

The following assumptions are considered: (i) $\mathbf{f} \cdot \mathbf{b}_1 = 0 \; \forall s \in (0, \ell)$; (ii) the rotations of the cross sections are sufficiently small, $|\theta| \ll 1$; (iii) rotary inertia is negligible. One direct consequence of hypothesis (i) is that, under the prevailing assumption of axially restrained motion, the longitudinal inertia term $(\rho A \partial_{tt} \boldsymbol{u} \cdot \mathbf{b}_1)$ is negligible in Eq. (53). Moreover, the load-bearing contribution associated with the shear force, $\kappa \partial_s M / \nu$, is of higher order with respect to the tension gradient in Eq. (53). Thus, Eq. (53) yields $\partial_s N = 0$ whose consequence is that the tension is constant throughout the beam, within the range of validity of the stated assumptions. The beam elongation $\epsilon = \nu - 1$ can be expanded in Taylor series up to second-order terms as $\epsilon(s, t) = \partial_s u + 1/2(\partial_s v)^2$. We make an important assumption that the elongations caused by the transverse motion are sufficiently small that the constitutive law for the tension is considered within the linear range as $N(s, t) = E^{(1)} A \epsilon(s, t) = E^{(1)} A [\partial_s u + 1/2(\partial_s v)]$. The uniformity of N allows its computation as an average over the span $[0, \ell]$:

$$\hat{N}(t) = \frac{1}{\ell} \int_0^\ell E^{(1)} A \left[\partial_s u + \tfrac{1}{2} (\partial_s v)^2 \right] ds \\ = \frac{E^{(1)} A}{\ell} [u(\ell, t) - u(0, t)] + \frac{E^{(1)} A}{\ell} \int_0^\ell \tfrac{1}{2} (\partial_s v)^2 ds \quad (56)$$

where uniform properties of the beam are considered (i.e., $E^{(1)} A = $ const) and $u(\ell, t) = u(0, t) = 0$ is the typical kinematic boundary condition for hinged–hinged or clamed–clamped or hinged–clamped beams.

The next step is to consider the equation of motion in the transverse direction (54) by introducing the following approximations: $\partial_s (\partial_s M / \nu) \sim \partial_{ss} M$, $\mathbf{f} \cdot \mathbf{b}_1 \sim \mathbf{f} \cdot \mathbf{e}_1 = f$, $\rho A \partial_{tt} \mathbf{r} \cdot \mathbf{b}_1 \sim \rho A (\partial_{tt} y + \partial_{tt} v)$, and $\kappa N \sim (\partial_{ss} v) N$ where the linear part of the bending curvature $\kappa = \partial_{ss} v$ was used in order to retain only leading order terms. Substituting in Eq. (54) the nonlinear hysteretic moment–curvature constitutive relationship for M given by (16) and (17) yields the equation of motion given by Eq. (18).

Inextensible beams. Reconsidering the equations of motion (53)–(55), the model is specialized to incorporate the shear undeformability and longitudinal inextensibility constraints putting $\eta = 0$ and $\nu = 1$. The above material constraints entail the following kinematic relationships [11]:

$$\partial_s u = -1 + \sqrt{1 - (\partial_s v)^2}, \quad \kappa = \frac{\partial_{ss} v}{\sqrt{1 - (\partial_s v)^2}}, \quad (57)$$

$$u(s, t) = -s + \int_0^s \left(\sqrt{1 - (\partial_s v)^2} \right) ds, \\ \cos \theta = 1 + \partial_s u, \quad \sin \theta = \partial_s v. \quad (58)$$

A condensation procedure is enforced to eliminate from the equations of motion the reactive shear force Q and tension N. To this end, the rotary inertia term $\rho J \partial_{tt} \theta$ is neglected. We further assume that $\mathbf{f} \cdot \mathbf{b}_1 \sim f$ and $\mathbf{f} \cdot \mathbf{b}_3 \sim 0$. From the balance of angular momentum expressed by Eq. (55), the shear force Q is explicitly solved for to give $Q = -\partial_s M$. In turn, this expression is substituted into Eqs. (53) and (54). On the other hand, Eq. (53) can be solved for $\partial_s N$ which, upon integration, gives

$$N(s, t) = N(\ell, t) - \int_s^\ell [\kappa Q + \rho A (\partial_{tt} u \cos \theta \\ + (\partial_{tt} y + \partial_{tt} v) \sin \theta)] d\xi, \quad (59)$$

where $N(\ell, t) = 0$ for a free end.
Substituting the obtained tension N into Eq. (54) provides the reduced equation of motion [11]

$$\rho A(\partial_{tt} v \cos\theta - \partial_{tt} u \sin\theta) + \kappa \int_s^\ell [\rho A(\partial_{tt} u \cos\theta$$
$$+\partial_{tt} v \sin\theta) - \kappa \partial_s M]\, d\xi$$
$$+\partial_{ss} M = f - \rho A\, \partial_{tt} y \cos\theta$$
$$-\kappa \int_s^\ell \rho A \partial_{tt} y \sin\theta\, d\xi \tag{60}$$

which is further transformed once the longitudinal displacement u is expressed in terms of the deflection v. An approximate mechanical model can be obtained by expressing in Taylor series the kinematic relationships. By considering the following third-order approximations:

$$\sin\theta \cong \partial_s v, \quad \cos\theta \cong 1 - \tfrac{1}{2}(\partial_s v)^2,$$
$$\kappa \cong \partial_{ss} v + \tfrac{1}{2}(\partial_s v)^2 \partial_{ss} v,$$
$$u \cong -\int_0^s \tfrac{1}{2}(\partial_s v)^2\, ds,$$
$$\partial_t u \cong -\int_0^s \partial_s v \partial_{st} v\, ds,$$
$$\partial_{tt} u \cong -\int_0^s \left[\partial_s v \partial_{stt} v + (\partial_{st} v)^2\right] ds \tag{61}$$

the obtained equation of motion is (21) where the leading order term only was retained in the base excitation expression, namely, $\rho A\, \partial_{tt} y \cos\theta - \kappa \int_s^\ell \varrho A \partial_{tt} y \sin\theta\, d\xi \simeq \rho A\, \partial_{tt} y$.

Coefficients in the reduced-order model of hinged–hinged beams

$$k_1 = \frac{E^{(1)} J}{\ell} \mathcal{D}\left[\phi''''\right] = \frac{E^{(1)} J}{\ell} n^4 \pi^4$$
$$k_3 = \frac{E^{(1)} J}{\ell} \mathcal{D}\left[(\phi'')^3 + \frac{1}{2}(\phi')^2 \phi'''' + 3\,\phi'\phi''\phi'''\right]$$
$$= k_1 \frac{(n\pi)^2}{4}$$
$$k_{z2} = 2 \frac{E^{(1)} J}{\ell^2} \mathcal{D}\left[(\phi''')^2 + \phi''\phi''''\right]$$
$$= 2 \frac{k_1}{\ell} \frac{2}{3}\sqrt{2}\pi n \left(1 - (-1)^n\right)$$
$$-4\left((-1)^n + 2\right)\sin^4\left(\frac{\pi n}{2}\right))$$
$$k_{z3} = 3 \frac{E^{(1)} J}{\ell^3} \mathcal{D}\left[\phi''\left(2(\phi''')^2 + \phi''\phi''''\right)\right]$$
$$= 3 \frac{\bar{k}}{\ell^2} \frac{(n\pi)^4}{2}$$

Operators and coefficients in the reduced-order model of cantilever beams

$$\mathcal{I}_1(s^*) = \Big[4c_\lambda^2 \lambda s^* + (c_\lambda^2 - 1)\sin(2\lambda s^*) + c_\lambda^2 \sinh(2\lambda s^*)$$
$$- 4(c_\lambda^2 + 1)\cos(\lambda s^*)\sinh(\lambda s^*)$$
$$+ 4\cosh(\lambda s^*)\left(2c_\lambda \cos(\lambda s^*)\right.$$
$$\left. -(c_\lambda^2 - 1)\sin(\lambda s^*)\right)$$
$$- 2c_\lambda \cos(2\lambda s^*) - 2c_\lambda \cosh(2\lambda s^*)$$
$$- 4c_\lambda + \sinh(2\lambda s^*)\Big],$$
$$\mathcal{I}_2(s^*) = 2c_\lambda(\sin(2\lambda s^*) - \sin(2\lambda))$$
$$+ 4c_\lambda \sinh(\lambda)(\cos(\lambda) - c_\lambda \sin(\lambda))$$
$$+ 4(\cosh(\lambda s^*) - \cosh(\lambda))(c_\lambda(\sinh(\lambda)$$
$$- \sin(\lambda)) + \cos(\lambda))$$
$$+ 4c_\lambda \sinh(\lambda s^*)(c_\lambda \sin(\lambda s^*) - \cos(\lambda s^*)),$$
$$\mathcal{I}_3(s^*) = 8(c_\lambda \sinh(\lambda)(c_\lambda \sin(\lambda) - \cos(\lambda))$$
$$+ \cosh(\lambda)(\cos(\lambda) - c_\lambda \sin(\lambda))$$
$$+ c_\lambda \sinh(\lambda s^*)(\cos(\lambda s^*) - c_\lambda \sin(\lambda s^*))$$
$$+ \cosh(\lambda s^*)(c_\lambda \sin(\lambda s^*) - \cos(\lambda s^*))),$$
$$\bar{k} = \frac{E^{(1)} J}{\ell} \mathcal{D}\left[\phi''''\right] \equiv \lambda_1^4 \frac{E^{(1)} J}{\ell},$$
$$k_3 = \frac{E^{(1)} J}{\ell} \mathcal{D}\Big[(\phi'')^3 + \frac{1}{2}(\phi')^2 \phi''''$$
$$+ 3\,\phi'\phi''\phi''' - \phi'' \int_s^1 \phi''\phi'''\Big] := \frac{\bar{k}}{\lambda_1^4} s_3,$$
$$k_{z2} = 2 \frac{E^{(1)} J}{\ell^2} \mathcal{D}\left[(\phi''')^2 + \phi''\phi''''\right] := \frac{2\bar{k}}{\lambda_1^4 \ell} s_{z2},$$
$$k_{z3} = 3 \frac{E^{(1)} J}{\ell^3} \mathcal{D}\left[\phi''\left(2(\phi''')^2 + \phi''\phi''''\right)\right]$$
$$:= \frac{3\bar{k}}{\lambda_1^4 \ell^2} s_{z3}.$$

References

1. Li, X., Song, M., Yang, J., Kitipornchai, S.: Primary and secondary resonances of functionally graded graphene platelet-reinforced nanocomposite beams. Nonlinear Dyn. **95**, 1807–1826 (2018)
2. Cetraro, M., Lacarbonara, W., Formica, G.: Nonlinear dynamic response of carbon nanotube nanocomposite microbeams. J. Comput. Nonlinear Dyn. **12**, 031007 (2017)
3. Rokni, H., Milani, A.S., Seethaler, R.J.: Size-dependent vibration behavior of functionally graded CNT-reinforced polymer microcantilevers: modeling and optimization. Eur. J. Mech. A Solid **49**, 26–34 (2015)
4. Yas, M.H., Heshmati, M.: Dynamic analysis of functionally graded nanocomposite beams reinforced by randomly

oriented carbon nanotube under the action of moving load. Appl. Math. Modell. **36**(4), 1371–1394 (2012)

5. Formica, G., Lacarbonara, W., Alessi, R.: Vibrations of carbon nanotube-reinforced composites. J. Sound Vib. **329**, 1875–1889 (2010)

6. Talò, M., Lacarbonara, W., Formica, G., Lanzara, G.: Hysteresis identification of carbon nanotube composite beams. In: ASME 2018 International Design Engineering Technical Conferences and Computers and Information in Engineering Conference, pp. V004T08A021-V004T08A021. American Society of Mechanical Engineers (2018)

7. Lacarbonara, W., Talò, M., Carboni, B., Lanzara, G.: Tailoring of hysteresis across different material scales. In: Belhaq, M. (ed.) Recent Trends in Applied Nonlinear Mechanics and Physics, pp. 227–250. Springer, Cham (2018)

8. Koratkar, N.A., Suhr, J., Joshi, A., Kane, R.S., Schadler, L.S., Ajayan, P.M., Bartolucci, S.: Characterizing energy dissipation in single-walled carbon nanotube polycarbonate composites. Appl. Phys. Lett. **87**(6), 063102 (2005)

9. Suhr, J., Koratkar, N.A.: Energy dissipation in carbon nanotube composites: a review. J. Mater. Sci. **43**(13), 4370–4382 (2008)

10. Carboni, B., Lacarbonara, W., Brewick, P.T., Masri, S.F.: Dynamical response identification of a class of nonlinear hysteretic systems. J. Intel. Mat. Syst. Str. **29**(13), 2795–2810 (2018)

11. Lacarbonara, W.: Nonlinear Structural Mechanics Theory, Dynamical Phenomena, and Modeling. Springer, New York (2013)

12. Talò, M., Carboni, B., Formica, G., Lanzara, G., Snyder, M., Lacarbonara, W.: Nonlinear dynamic response of nanocomposite cantilever beams. In: Proceedings of NODYCON 2019, Rome, February 17–20 (2019)

13. Formica, G., Talò, M., Lacarbonara, W.: Nonlinear modeling of carbon nanotube composites dissipation due to interfacial stick-slip. Int. J. Plast. **53**, 148–163 (2014)

14. Formica, G., Lacarbonara, W.: Three-dimensional modeling of interfacial stick-slip in carbon nanotube nanocomposites. Int. J. Plast. **88**, 204–217 (2017)

15. Formica, G., Taló, M., Lanzara, G., Lacarbonara, W.: Modeling and identification of carbon nanotube nanocomposites constitutive response. J. Appl. Mech. **86**(4), 041007 (2019)

16. Lacarbonara, W., Arena, A., Antman, S.S.: Flexural vibrations of nonlinearly elastic circular rings. Meccanica **50**, 689–705 (2015)

17. Nayfeh, A., Mook, D.: Nonlinear Oscil. Wiley, London (1995)

18. Rega, G., Lacarbonara, W., Nayfeh, A., Chin, C.: Multiple resonance in suspended cables: direct versus reduced-order models. Int. J. NonLinear Mech. **34**, 901–924 (1999)

19. Lacarbonara, W., Rega, G., Nayfeh, A.: Resonant non-linear normal modes. Part I: analytical treatment for structural one-dimensional systems. Int. J. NonLinear Mech. **38**, 851–872 (2003)

20. Casalotti, A., Lacarbonara, W.: Nonlinear vibration absorber optimal design via asymptotic approach. In: P. Hagedorn (ed.), Proceedings of the IUTAM Symposium on Analytical Methods in Nonlinear Dynamics, vol. 19, pp. 65–74. Elsevier (2016)

21. Casalotti, A., Lacarbonara, W.: Tailoring of pinched hysteresis for nonlinear vibration absorption via asymptotic analysis. Int. J. NonLinear Mech. **94**, 59–71 (2016)

22. Caughey, T.: Random excitation of a system with bilinear hysteresis. J. Appl. Mech. **27**(4), 649–652 (1960)

23. Jennings, P.: Periodic response of a general yielding structure. J. Eng. Mech. ASCE **90**(2), 131–166 (1964)

24. Baber, T.T., Wen, Y.K.: Random vibration of hysteretic degrading systems. J. Eng. Mech. ASCE **107**, 1069–1087 (1981)

25. Iwan, W.: A distributed-element model for hysteresis and its steady-state dynamic response. J. Appl. Mech. **33**, 893–900 (1966)

26. Bouc, R.: Forced vibration of mechanical systems with hysteresis. In: 4th Conference on Nonlinear Oscillation, Prague, Czechoslovakia (1967)

27. Iwan, W., Lutes, L.: Response of the bilinear hysteretic system to stationary random excitation. J. Acoust. Soc. Am. **43**, 545–552 (1968)

28. Masri, S.: Forced vibration of the damped bilinear hysteretic oscillator. J. Acoust. Soc. Am. **57**, 106–113 (1975)

29. Wen, Y.: Method for random vibration of hysteretic systems. J. Eng. Mech. ASCE **102**, 249–263 (1976)

30. Capecchi, D., Vestroni, F.: Periodic response of a class of hysteretic oscillators. Int. J. NonLinear Mech. **25**, 309–317 (1990)

31. Wen, Y.: Equivalent linearization for hysteretic systems under random excitation. J. Appl. Mech. **47**, 150–154 (1980)

32. Lacarbonara, W., Vestroni, F.: Nonclassical responses of oscillators with hysteresis. Nonlinear Dyn. **32**, 235–258 (2003)

33. Vinogradoc, O., Pivovarov, L.: Vibrations of a system with nonlinear hysteresis. J. Sound Vib. **111**, 145–152 (1986)

34. Yar, M., Hammond, J.: Modeling and response of bilinear hysteretic systems. J. Eng. Mech. ASCE **113**, 1000–1013 (1987)

35. Masri, S., Miller, R., Traina, M., Caughey, T.: Development of bearing friction models from experimental measurements. J. Sound Vib. **148**, 455–475 (1991)

36. Casini, P., Vestroni, F.: Nonlinear resonances of hysteretic oscillators. Acta Mech. **229**(2), 939–952 (2018)

37. Vestroni, F., Casini, P.: Mitigation of structural vibrations by hysteretic oscillators in internal resonance. Nonlinear Dyn. (2019). https://doi.org/10.1007/s11071-019-05129-9

38. Bernardini, D., Vestroni, F.: Non-isothermal oscillations of pseudoelastic devices. Int. J. NonLinear Mech. **38**(9), 1297–1313 (2003)

39. Lacarbonara, W., Bernardini, D., Vestroni, F.: Nonlinear thermomechanical oscillations of shape-memory devices. Int. J. Solids Struct. **41**, 1209–1234 (2004)

40. Formica, G., Milicchio, F., Lacarbonara, W.: Hysteretic damping optimization in carbon nanotube nanocomposites. Compos. Struct. **194**, 633–642 (2018)

41. Formica, G., Milicchio, F., Lacarbonara, W.: Computational efficiency and accuracy of sequential non-linear cyclic analysis of carbon nanotube nanocomposites. Adv. Eng. Softw. **125**, 126–135 (2018)

42. Talò, M., Krause, B., Pionteck, J., Lanzara, G., Lacarbonara, W.: An updated micromechanical model based on morphological characterization of carbon nanotube nanocomposites. Compos. Part B Eng. **115**, 70–78 (2017)

43. Hill, R.: A self-consistent mechanics of composite materials. J. Mech. Phys. Solids **13**, 213–222 (1965)
44. Lacarbonara, W.: Direct treatment and discretizations of non-linear spatially continuous systems. J. Sound Vib. **221**, 849–866 (1998)
45. Golubitsky, M., Schaeffer, D.G.: Singularities and groups in bifurcation theory. In: Applied Mathematical Sciences, vol. 51. Springer (1985)
46. Hill, T.L., Neild, S.A., Cammarano, A.: An analytical approach for detecting isolated periodic solution branches in weakly nonlinear structures. J. Sound Vib. **379**, 150–165 (2016)
47. Habib, G., Cirillo, G.I., Kerschen, G.: Uncovering detached resonance curves in single-degree-of-freedom systems. Proc. Eng. **199**, 649–656 (2017)
48. Detroux, T., Noël, J.-P., Virgin, L.N., Kerschen, G.: Experimental study of isolas in nonlinear systems featuring modal interactions. Plos One **13**(3), e0194452 (2018)
49. Haller, G., Ponsioen, S.: Nonlinear normal modes and spectral submanifolds: existence, uniqueness and use in model reduction. Nonlinear Dyn. **86**(3), 1493–1534 (2016)
50. Ponsioen, S., Pedergnana, T., Haller, G.: Analytic prediction of isolated forced response curves from spectral submanifolds. Nonlinear Dyn. (2019). https://doi.org/10.1007/s11071-019-05023-4